One and Two Neutron Removal Cross-Sections of ^{24}O via Projectile Fragmentation

A dissertation presented to

the faculty of

the College of Arts and Sciences of Ohio University

In partial fulfillment

of the requirements for the degree

Doctor of Philosophy

Dilupama A. Divaratne

May 2014

This dissertation titled

One and Two Neutron Removal Cross-Sections of ^{24}O via Projectile Fragmentation

by

DILUPAMA A. DIVARATNE

has been approved for

the Department of Physics and Astronomy

and the College of Arts and Sciences by

Carl R. Brune

Professor of Physics and Astronomy

Robert Frank

Dean of the College of Arts and Sciences

ABSTRACT

DIVARATNE, DILUPAMA A., Ph.D., May 2014, Physics

Director of Dissertation: Carl R. Brune

The objective of this research work is to study the ground state wave-function of ^{24}O, building on recent work conducted on this topic by various experimentalists and theorists. The ultimate goal is to investigate how exactly doubly magic ^{24}O is. Motivated by observations and guided by theoretical perspectives applicable to nuclear structures of neutron rich isotopes, the cross section and related spectroscopic factors to the different final states in ^{23}O are employed to investigate the ground sate wave function of ^{24}O. The experiment was conducted at the National Superconducting Cyclotron Laboratory in Michigan State University using the S800 spectrograph and 470 mg/cm^2 Be reaction target with 92.3 MeV/u ^{24}O beam energy. It measured the neutron knockout cross section of ^{24}O to the $1/2^+$ ground state of ^{23}O and two neutron removal cross section to ^{22}O. However, in this experiment, the neutron in the latter was not measured using the neutron detector. The cross section values to the different final states of ^{23}O along with the related spectroscopic factors convey to us the composition of the ^{24}O ground state wave function and eventually the magicity of it. Specific details of the experiment, analysis carried out to measure the neutron knockout cross sections and longitudinal momentum distributions of residual, and interpretation and physics justification of the resulting cross sections and longitudinal momenta both in lab frame and projectile rest frame are discussed herein.

For the one who was waiting for this day, The one who still lights up my way,

My strength, My courage,

The one who saw me as his successor, his pride,

My loving Appachchi (Daddy)

This one is for you.

ACKNOWLEDGMENTS

the academic advisor, Dr. Daniel Philips and all the faculty members of the Department of Physics and Astronomy.

My heartiest gratitude goes to my loving husband, Harsha, for continuous support and encouragement given throughout this journey we share together. You taught me a lot and made me a better researcher by being the strength behind my success in everything I do. Special thanks to our little baby girl, Minsara, for the immense patience and giving mommy the time to work. The need to be with you motivated me to work harder. A warm gratitude to my loving ammi (mommy) for all your silent prayers, wishes, celebrations and tears fallen for me. Your love is the best thing that ever happened to me and I know I will have it for the rest of my life. You fed me, believed in me and made me the person who I am today. Words just can't say how lucky I am to have two wonderful big sisters in my life. Its a blessing I carry with me for life. Kitty and Ditty, you make my life more beautiful and bright every single day. I would also like to extend heartiest gratitude to my loving parents-in-law for being another mom and dad to me and for all your efforts to free me from house hold duties, and my brothers, Sampath, Dilum, and Vida for the constant encouragement and support. I would like to extend my love to all our Sri Lankan fiends in Athens and Columbus, and all my colleagues in the Department of Physics for being such great, caring and loving friends. My family and friends are the builders of my personality and self-confidence which give me the strength to climb up each step of life with great ambitions.

TABLE OF CONTENTS

LIST OF TABLES

LIST OF FIGURES

1 INTRODUCTION

1.1 Motivation

When considering the standard model of particle physics, the protons and neutrons are made of particles called quarks which interact with one another inside the nucleons. However, when studying nuclei, which are made up of nucleons, the better approach is to consider these interactions as an effective interaction, the interaction between individual nucleons. These nuclear interactions between proton and proton are similar to the interaction of neutron-neutron and proton-neutron. The only difference is that different nucleons, protons and neutrons, have different isospin states. The behavior of these nucleons inside a nucleus is pictured through many theoretical models such as the shell model [Bro01] which describe the interaction of quantum many body systems.

Understanding the wave functions of neutron-rich isotopes will provide a strong base for understanding the structure of other nearby neutron rich isotopes and will add a bench mark to the growing knowledge of nuclear structure physics which started with the discovery of the neutron as a fundamental particle by Chadwick in 1932. Understanding the three fundamental forces (namely, the strong force that is responsible for the binding of nuclei together, the weak force that converts protons to charge-less neutrons and the electromagnetic force that makes positively charged protons repel each other) through structure experiments of this kind provides a better landscape for growing a complete understanding of all the nuclei interactions and thus may lead to quantum mechanical discoveries.

The establishment of the ground state wave function of ^{24}O will be advantageous to understand nuclear structure of isotopes near the drip line which have unusual proton to neutron ratios. The results of this research will build a foundation for a variety of other experiments to explore more about the isotopes that have only been investigated by theory.

Neutron-rich doubly magic nuclei in which the protons and neutrons are arranged into complete shells within the atomic nucleus, and other nuclei near the neutron drip line continue to intrigue nuclear physicists.

1.2   Goal of the experiment

The goal of the experiment is to measure the cross section for neutron knockout from ^{24}O to the ground state of ^{23}O and to the first excited state of ^{23}O. The purpose of the study is to get a deeper understanding of ^{24}O being doubly magic with closed $\nu(0d_{5/2})^6$ and $\nu(1s_{1/2})^2$ sub shells. RIKEN has already completed a set of experiments to identify the two higher excited states of ^{23}O and the energy gap between $\nu(1s_{1/2})$ and $\nu(0d_{3/2})$ orbitals in ^{23}O [KT10]. With these results, the next step is to determine the composition of the ground state wave function of ^{24}O. In the current experiment, the longitudinal momentum distribution could be constructed for each final state identified in the n-^{22}O invariant mass spectrum. This will give information on the orbital angular momentum and thus of the spin parity of the knocked out neutron and the spectroscopic overlap of the ^{23}O excited state with the ^{24}O ground state. The shape of the longitudinal momentum distribution would indicate how the neutron wave functions for the $1s_{1/2}$ and $0d_{5/2}$ orbitals are expected to be. Together, the results for the neutron knockout cross sections of ^{24}O to the ground state of ^{23}O and to the first excited state of ^{23}O along with other spectroscopic factors will lead to a complete understanding of the ^{24}O ground state wave function and this will in turn provide an indication of how doubly magic ^{24}O really is.

1.3   Theory behind the experiment

With the recent discovery of ^{24}O [Hof09], the next step is to establish the composition of its ground state wave function. The ^{24}O isotope has 8 protons and 16 neutrons. We know how 8 protons and 8 neutrons arrange in shells but there are many ways to fill the levels with the remaining 8 neutrons. Depending on how the neutrons get excited within

the model, different spin states are created with different energies. In the single particle model, we can create many different states. If we consider only the 0^+ spin states, they will mix due to the residual two-body interaction. It will be possible to find their eigen-energy values by diagonalizing the matrix produced by the Hamiltonian consisting of one body and two body matrix elements. The real eigenstate is a linear combination of all those 0^+ single-particle states of ^{24}O which will be the ground state of ^{24}O.

Figure 1.1 shows the evolution of the effective single particle energies (ESPE) as function of neutron number in heavy oxygen isotopes using the USD (universal s-d shell model) interaction [Bro01]. Effective single particle energies are a combination of single particle energies and diagonal two body matrix elements. This provides a magic nature to the heavy oxygen isotopes. ^{22}O is found to be doubly magic because of the large energy gap between the empty $\nu(1s_{1/2})$ and full $\nu(1d_{5/2})$ sub-shells at N=14. For N=16 the gap between filled $\nu(1s_{1/2})$ and empty $\nu(0d_{3/2})$ sub-shells should be sufficiently large enough to make ^{24}O a doubly magic nucleus [KT10]. Figure 1.2 provides the experimental and theoretical level scheme of heavy oxygen isotopes [EDA$^+$07, SFB$^+$07].
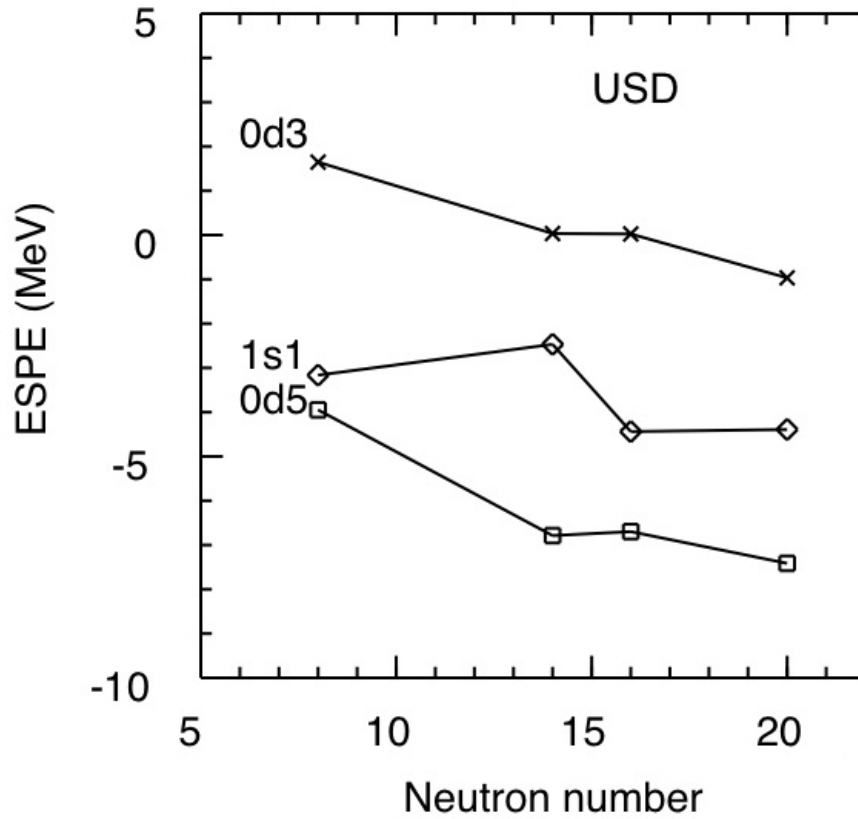
Figure 1.1: Evolution of effective single-particle energies (ESPE) in the Universal s-d Shell Model, as a function of neutron number for heavy oxygen isotopes. Figure taken from [Bro01].

The two planned experiments will measure the neutron knockout cross section of ^{24}O to the $1/2^+$ ground state of ^{23}O (in the first experiment) and to the neutron unbound $5/2^+$ first excited state of ^{23}O (in the second experiment). These cross section values to the different final states of ^{23}O along with the related spectroscopic factors will convey the composition of the ^{24}O ground state wave function and eventually its magicity. Therefore the results of the two proposed experiments will lead to a conclusion about how doubly magic ^{24}O really is.
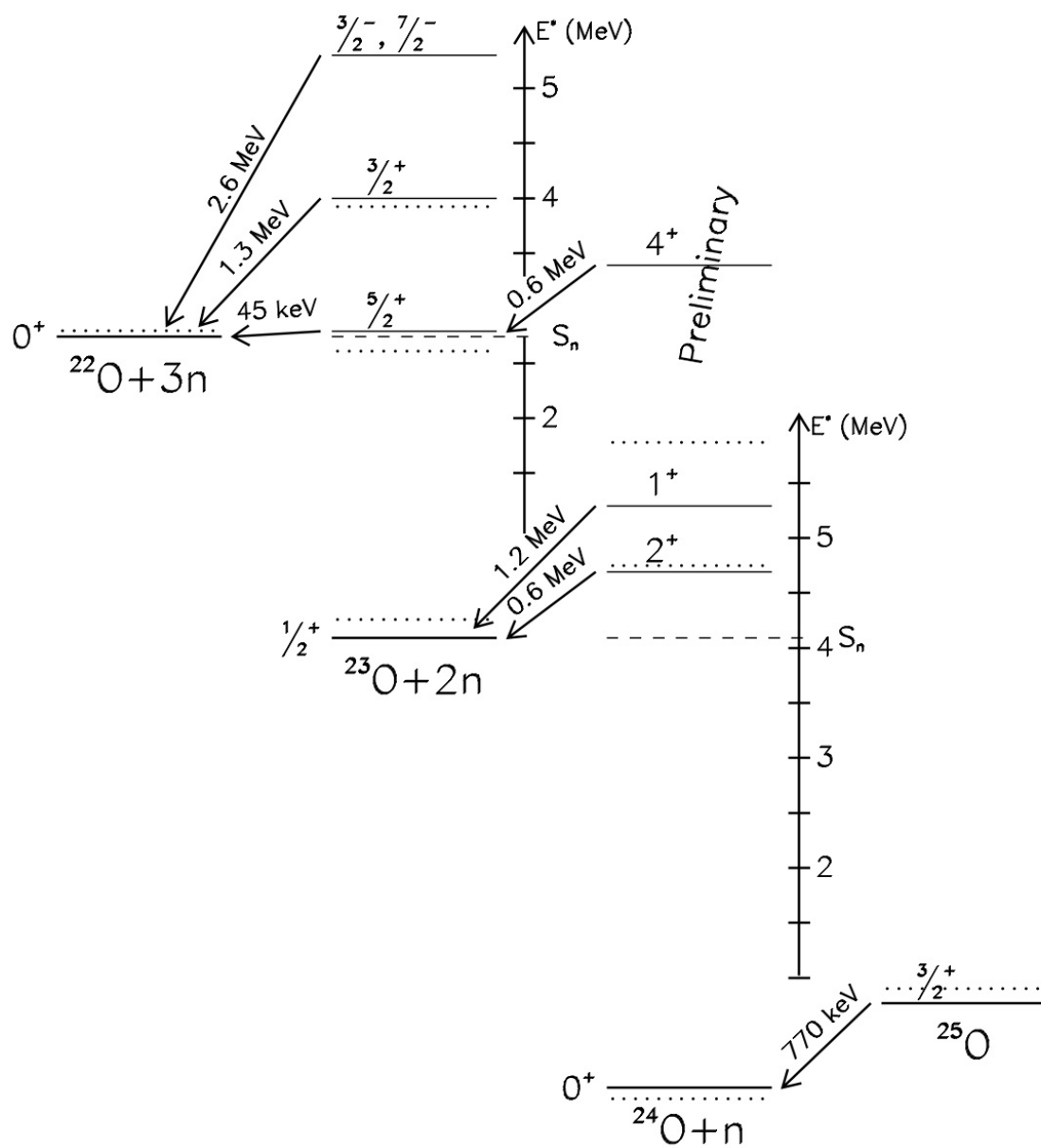
Figure 1.2: Experimentally discovered energy levels (solid lines) and theoretically predicted energies using shell model calculations (dotted lines) of heavy oxygen isotopes, ^{24}O, ^{23}O and ^{22}O [EDA$^+$07, SFB$^+$07]

2 THEORETICAL TREATMENT

The theoretical background behind this experimental work is described in the first section of this chapter by explaining the theoretical models which describe the nuclear structure and single particle excitations within that model. A brief introduction about the atomic shell structure is also included in the section to provide an overview of what models were available for atoms before the nuclear shell model came into play. The idea of the first nuclear shell model was formed upon the verification of the successful atomic electron shell model and various experimental observations made by the1963 Physics Nobel prize winner Maria Goeppert-Mayer [May48]. The final section of this chapter explains one and two nucleon removal reactions and rare isotope beam production mechanisms.

2.1 Atomic Shell Structure

The electrons in the atom circulate around the nucleus in exact energy levels and it is known that no two electrons in a single atom can not occupy the same energy level (Pauli Exclusion Principle). In other words no two electrons can have same four quantum numbers, n, l, m_l and m_s. Just like the electron can be excited and kicked out from an atom by providing energy, a neutron or a proton can also be removed from a nucleus but they have a much larger binding energy than above (in MeV range as oppose to eV range in ionization energies). This is due to the strong nuclear force that keeps the nucleons strongly bound to each other inside the nucleus. When considering the energy needed to knockout an electron from a shell for all the elements, noble gasses require higher energies than other elements [Bro01]. This is because of the complete shells these inert gasses have which make them binding stronger to the nucleus. Figure 2.1 shows a diagram which gives the first ionization energies of the elements in the periodic table [bri].
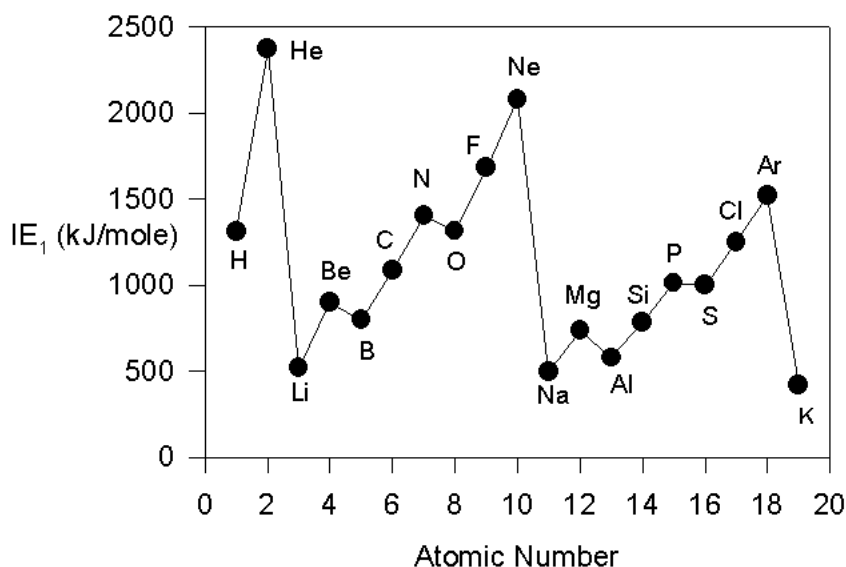
Figure 2.1:   First ionization energies of the elements in the periodic table. Figure taken from [bri].

According to the rules in filling up the orbitals, the magic numbers for electrons in an atom are easy to extract (see Table 2.1). When there are 2 electrons in the atom, the $n=1$ shell is completely filled thus 2 acts as the first magic number. When there are 10 electrons, the first two fill the $n=1$ orbital and the remaining 8 completely fill the $n=2$ orbital being the second magic number for electrons. Likewise 28 will be the next magic number. Depending on their single particle energy levels and spin orbit coupling, nucleons can also possess a magic nature. Studying how and what magic numbers they can acquire is important in understanding the nuclear structure of neutron and proton rich isotopes near the drip line.

Table 2.1: Selection rule, allowed values for four quantum numbers of electrons in an atom, and building up of magic numbers [mag]. Note that the table is showing the selection rule only up to $n=6$.

n	l	m_l	Orbital	Elements	Total	Shell
$n=1$	0	0	$1s$	2	2	K
$n=2$	0	0	$2s$	2	8	L
	1	-1,0,1	$2p$	6		
$n=3$	0	0	$3s$	2	18	M
	1	-1,0,1	$3p$	6		
	2	-2,-1,0-1,2	$3d$	10		
$n=4$	0	0	$4s$	2	32	N
	1	-1,0,1	$4p$	6		
	2	-2,-1,0-1,2	$4d$	10		
	3	-3,-2,-1,0,1,2,3	$4f$	14		
$n=5$	0	0	$5s$	2	32	O
	1	-1,0,1	$5p$	6		
	2	-2,-1,0-1,2	$5d$	10		
	3	-3,-2,-1,0,1,2,3	$5f$	14		
	4	-4,-3,-2,-1 0,1,2,3,4	$5g$	18	Unknown Elements	
$n=6$	0	0	$6s$	2	18	P
	1	-1,0,1	$6p$	6		
	2	-2,-1,0-1,2	$6d$	10		
	3	-3,-2,-1,0,1,2,3	$6f$	14	Unknown Elements	
	4	-4,-3,-2,-1,0,1,2,3,4	$6g$	18	Unknown Elements	
	5	-5,-4,-3,-2,-1,0,1,2,3,4,5	$6h$	22	Unknown Elements	

2.2 The Nuclear Shell Model

The nuclear shell model is a phenomenological model which describe the arrangement of nucleons inside a nucleus [Bro01]. The origin of the Shell Model is the observation that there are certain magic numbers of nucleons which are more tightly bound than the next

higher number. When adding protons or neutrons to the nucleus, there are certain occasions where the binding energy of the next nucleon is significantly less than the last one. See Figure 2.2. This magic nature of some nuclei and some other properties can be explained by the nuclear Shell Model by approximating it with three dimensional harmonic oscillator potential and spin-orbit coupling. In describing the mean field potential for the nucleons inside the nucleus, the Woods-Saxon potential approximately explains the forces applied on each proton and neutron. Spin-orbit coupling is an interaction between particle's motion with its spin. In nucleons, spin-orbit interaction describes a coupling effect between the angular momentum and the strong nuclear force of the nucleons moving inside the nucleus.

Figure 2.2 shows a graph with single nucleon separation energies for even-even nuclei for $N>Z$ (in the top figure) and difference between the neutron separation energies for the same set of nuclei (in the bottom figure) [Bro].
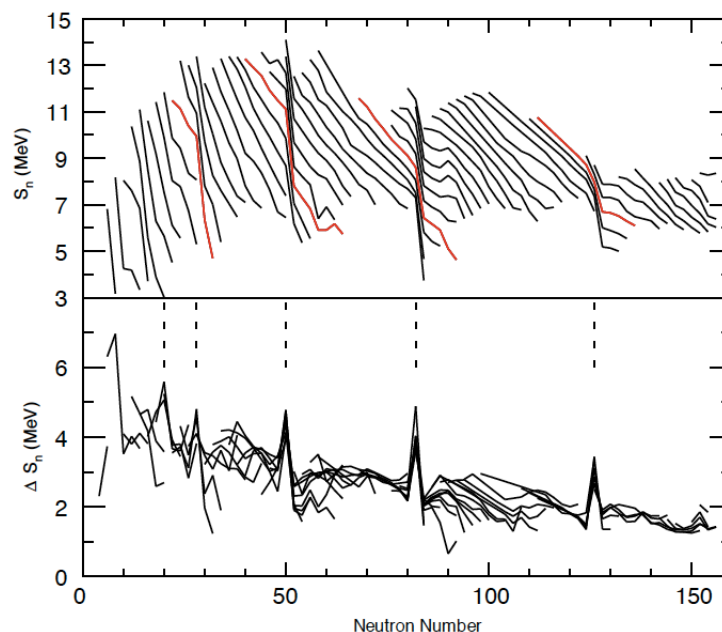
Figure 2.2: Single nucleon separation energies for even-even nuclei for $n>z$ (in the top figure) and difference between the neutron separation energies for the same set of nuclei (in the bottom figure). Figure taken from [Bro]

The Universal *sd*-shell model (USD) in the nuclear region in which it can be applied have shown a good amount of agreement with experimental measurements compared to other available shell models. This USD shell model is kind of a phenomenological model with a truncated *sd*-shell in which any nucleon wave function outside of the *sd*-shell is neglected.

Nucleons inside a nucleus are subjected to a mean potential and the single particle motion inside this potential can be solved by obtaining the eigenstates which are called orbits. These eigen values are single particle energies occupied by the nucleons. The potential is assumed to be spherical and is in the shape of a Wood-Saxon potential. This is specified by three parameters: depth, radius, and diffuseness. A diagram explaining the Wood-Saxon potential varying with the distance from the center of the nucleus is in figure 2.3 [Ban09]. As it goes from the core of the nucleus to the edge, the potential or the force rapidly decreases and becomes zero just after the edge.
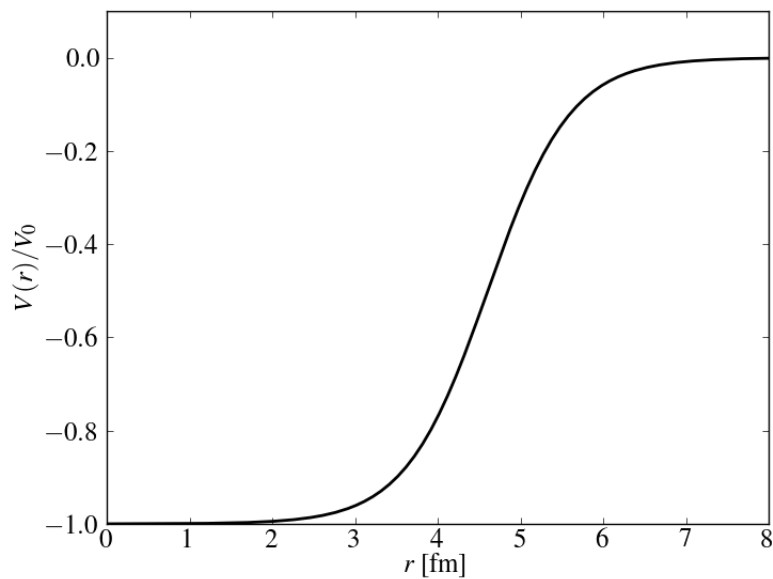
Figure 2.3: Variation of Wood-Saxon potential for A=50, at units of fermi, relative to V_0, a=0.5fm, with the distance from the center of the nucleus. Figure taken from [Ban09].

The Wood-Saxon potential is given by

$$V_0(r) = -\frac{V_0}{1 + \exp[r - R/a]} \tag{2.1}$$

where R=1.25A$^{1/3}$, with A being the number of nucleons inside the nucleus, a=0.65 fm and V_0 is in the order of 50 MeV. In order to give a more transparent description, the Wood-Saxon potential is overlaid with a harmonic oscillator potential. The harmonic oscillator potential can be described analytically and provide much simpler properties of eigenstates. The shell model is formed by adding a spin-orbit coupling to the harmonic oscillator potential to successfully reproduce experimental data. Adding the spin-orbit coupling make the degenerate orbits in the harmonic oscillator potential to split. This splitting of the energy levels is approximately proportional to the value of the angular momentum quantum number l and thus plays a significant role in predicting the nuclear magic numbers. The next section describe how this effect make some traditionally calculated magic numbers to disappear in the nuclear shell model to make new magic numbers.

2.2.1 Nuclear Magic Number

When considering the removal of single proton or a neutron from a nucleus, the energy required have a similar shape with peaks in some elements and isotopes. These experimental evidences provide a clue that the neutrons and protons may be sitting in orbits just like electrons and some elements require higher nucleon removal energy when those have energy states that are completely filled. The nuclei which have a complete outer shell with protons or neutrons are called magic nuclei and the number of those protons and neutrons are called magic numbers. These experimental results are what gave rise to the idea of the nuclear shell model where neutrons and protons are held in a shell like structure instead of sitting inside the nucleus together. However not all the magic numbers computed using the shell closure are in accord with experimental results. To accurately

predict magic numbers, the spin-orbit interactions must be included in the shell model calculation. In nuclear shell model, the angular momentum quantum number l and spin quantum number s are coupled to give the total angular momentum quantum number j. The nucleon nucleon potential depends generally on s, l, and j with $j = l + s$. When it comes to protons and neutrons, the values allowed for the quantum numbers change due to the new total angular momentum quantum number, j, that arrises from combining the angular momentum quantum number and the spin quantum number. Unlike electrons the angular momentum quantum number l of protons and neutrons is not restricted by the value of n, the principal quantum number because there is really no physical analog to the principal quantum number n. In this case, the numbers associated with the level just start at $n=1$ for the lowest level associated with a given orbital quantum number. l in that manner can take any integer value starting from 1. Due to this reason, the total angular momentum quantum number j of protons and neutrons can have 1/2, 3/2, 5/2, 7/2 etc. This value of j determines the maximum number of protons and neutrons that can occupy a certain j orbital. Depending on the value of j, the maximum occupancy of protons or neutrons would be equal to $2j+1$. So for an example, the $1p^{3/2}$ sub-shell can be occupied by maximum of 4 protons or neutrons. There is an order to fill up the energy levels with protons or neutrons starting from the most tightly bound $1s^{1/2}$ energy level. The maximum occupancy of each level for protons or neutrons are the magic numbers [Kle01]. The system should be described using the quantum numbers j, m_j and parity instead of l, m_l and m_s. The Wood Saxon potential which reach to a constant at infinite distance is more realistic than the harmonic oscillator potential but the the actual average radius of the nucleon's orbit would be much larger. This effect results in a reduction in the energy levels of high l orbits because orbits with high average radii will have a lower energy. This is due to the deforming of the potential used to describe the shell structure of nucleons. Together with the spin-orbit coupling, these effects play a major role in predicting magic numbers for nucleons. Some

of the energy levels shift up and down according to the appropriate magnitudes of these effects and can be used to describe how the magic numbers 2, 8, 20, 28, 50, 82, 126 and 184 are formed. All first 6 magic numbers are experimentally observed and 126 and 184 are yet to be discovered through experiments. 24 and 34 have been predicted as new magic numbers emerging from recent experimental result [KT10]. The isotope of interest in this study ^{24}O was predicted to be a doubly magic (both proton number 8 and neutron number 16 being magic numbers) nucleus due to the sufficiently large energy gap between filled $\nu(1s_{1/2})$ and empty $\nu(0d_{3/2})$ sub-shells [KT10]. When the nuclei are magic, they tend to be more stable as it requires much more energy to remove a proton or a neutron from its completely filled orbitals than partially filled ones, which means that the binding energy is higher for magic nuclei than the other ones. This explains the discontinuities present in the single neutron separation energies of some elements as shown in Figure 2.2 [Bro].

2.2.2 Single particle excitations within the shell model

When the first excited states of some even-even nuclei are at a higher excitation energy compared to the other neighboring even-even nuclei, it indicates that the single-particle levels for both protons and neutrons have a larger energy gap. These values of Z and N are the magic numbers for protons and neutrons in the nuclear shell model. These nuclei are modeled by closed-shell configurations In the simplest approximation, nuclei which have large energy gap for only protons or neutrons will be called semi-magic nuclei whereas they are called doubly magic when the gap is large for both protons and neutrons in the closed shell configuration. Table 2.2 provides a list of those nuclei which have a higher excitation energy or a larger gap, along with the nominal closed-shell configuration [Bro01].

When considering the possible single particle excitations within the Shell Model, for ^{24}O isotope, the final single particle states and their spin configurations depend on how many particles from which spin state are excited to the $(0d_{3/2})$ empty state. The final

Table 2.2: Even-even nuclei with high-lying first excited states. The excitation energies are from the compilations [End90], [RBFZ96] except for ^{22}O from [TPB$^+$00], ^{24}O which is the theoretical USD value [she] and ^{34}Si from [IGB$^+$98]

Nucleus	Z	N	E_x (MeV)	J^π	Proton Configuration	Neutron Configuration
^{4}He	2	2	20.2	0^+	$(0s_{1/2})^2$	$(0s_{1/2})^2$
^{12}C	6	6	4.44	2^+	$(0s)^2(0p_{3/2})^4$	$(0s)^2(0p_{3/2})^4$
^{14}C	6	8	6.09	1^-	$(0s)^2(0p_{3/2})^4$	$(0s)^2(0p_{3/2})^4(0p_{1/2})^2$
^{16}O	8	8	6.05	0^+	$(0s)^2(0p)^6$	$(0s)^2(0p)^6$
^{22}O	8	14	3.17	2^+	$(0s)^2(0p)^6$	$(0s)^2(0p)^6(0d_{5/2})^6$
^{24}O	8	14	3.17	2^+	$(0s)^2(0p)^6$	$(0s)^2(0p)^6(0d_{5/2})^6$ $(1s_{1/2})^2$
^{34}Si	14	20	3.30	2^+	$(0s)^2(0p)^6(0d_{5/2})^6$	$(0s)^2(0p)^6(0d_{5/2})^6$ $(1s_{1/2})^2(0d_{3/2})^4$
^{42}Si	14	28	?		$(0s)^2(0p)^6(0d_{5/2})^6$	$(0s)^2(0p)^6(0d_{5/2})^6$ $(0d_{3/2})^4(0f_{7/2})^8(1s_{1/2})^2$
^{36}S	16	20	3.29	2^+	$(0s)^2(0p)^6(0d_{5/2})^6$ $(1s_{1/2})^2$	$(0s)^2(0p)^6(0d_{5/2})^6$ $(1s_{1/2})^2(0d_{3/2})^4$
^{40}Ca	20	20	3.35	0^+	$(0s)^2(0p)^6(0d1s)^{12}$	$(0s)^2(0p)^6(0d1s)^{12}$
^{48}Ca	20	28	3.83	2^+	$(0s)^2(0p)^6(0d1s)^{12}$	$(0s)^2(0p)^6$ $(0d1s)^{12}(0f_{7/2})^8$
^{56}Ni	28	28	2.70	2^+	$(0s)^2(0p)^6(0d1s)^{12}$ $(0f_{7/2})^8$	$(0s)^2(0p)^6$ $(0d1s)^{12}(0f_{7/2})^8$
^{52}Ca	20	32	2.56	2^+	$(0s)^2(0p)^6(0d1s)^{12}$	$(0s)^2(0p)^6(0d1s)^{12}$ $(0f_{7/2})^8(1p_{3/2})^4$
^{60}Ca	20	40	?		$(0s)^2(0p)^6(0d1s)^{12}$	$(0s)^2(0p)^6$ $(0d1s)^{12}(0f1p)^{20}$
^{70}Ca	20	50	?		$(0s)^2(0p)^6(0d1s)^{12}$	$(0s)^2(0p)^6(0d1s)^{12}$ $(0f1p)^{20}(0g_{9/2})^{10}$
^{68}Ni	28	40	1.77	0^+	$(0s)^2(0p)^6(0d1s)^{12}$ $(0f_{7/2})^8$	$(0s)^2(0p)^6$ $(0d1s)^{12}(0f1p)^{20}$

8 neutrons in ^{24}O are arranged in $1s_{1/2}$ and $0d_{5/2}$ sub-shells according to the maximum occupancy rules. There are five possible ways to excite neutrons from these sub-shells to the $(0d_{3/2})$ empty state such that the final spin configuration is in 0^+ state. Those are $(d_{3/2})^2 \times (d_{5/2})^{-2}$, $(d_{3/2})^2 \times (d_{5/2})^{-1} \times (s_{1/2})^{-1}$, $(d_{3/2})^2 \times (s_{1/2})^{-2}$ and 0^+ ground state. A 5×5 matrix can be formed from the above 5 states. This matrix can be diagonalized if each states can be described by single Slater determinant. The 0^+ states will be mixed due to the residual two body interactions. The two body matrix can be diagonalized to find the eigenfunctions and the correlated wave function.

2.3   One and Two Nucleon Removal Reactions

One and Two nucleon removal experiments play an important role in understanding the nuclear structure in the intermediate energy regime by studying the single particle states in rare nuclei. Nucleon-knockout reactions bring forward a complementary technique compared to gamma spectroscopic methods to measure the evolution of the positions and order of nuclear single-particle states in rare nuclei. It is also well suited for rare isotope beams produced using fragmentation [Tos01].

In single nucleon knockout reactions, events are typically identified by detecting the residual nuclei which travel with a velocity very close to the projectile beam. In most of these reactions, the state of the removed nucleon is unknown and not measured. The nucleon removal cross sections to the ground state of the residue nuclei is important in determining the wave function of the projectile using the single particle energy states extracted and the parallel momentum measured at the target. The cross sections for producing the reaction products in excited states are also now known to be very significant. The orbital angular momentum, l, and spectroscopic factor of the removed nucleon can be determined using the width of the measured longitudinal momentum distribution in the projectile rest frame and the cross section respectively [Tos01].

The single nucleon removal reactions are well explained by eikonal reaction theory together with shell model predictions and often produce comparable results with experiments [Sat12, KNP$^+$09]. The cross section calculation of the single nucleon knockout reaction of ^{24}O and the longitudinal momentum of ^{24}O to ^{23}O reaction in the projectile rest frame was directly compared with the calculations performed by using an eikonal reaction theory and shell-model spectroscopic factors [Sat12]. Quoting reference [Sat12] "The binding well geometry was fixed to reproduce the Hartree-Fock calculated binding energy and root-mean-square radius for each orbit in ^{24}O and ^{23}O".

In the most simple way, the case of direct two-nucleon removal reactions can be explained by describing the wave functions of the two removed nucleons in the projectile by studying the product of nucleon wave functions in the single-particle orbitals to take the two nucleons to be uncorrelated, other than both being bound to the same core [BBC$^+$03, Tos07]. The longitudinal momentum distribution of the two nucleons provide their quantum numbers. The longitudinal momentum of the residue will be the convolution of those momenta of the two nucleons but it is important to account for the total angular momentum coupling of the two nucleons when producing the final states of the residue [Tos07].

2.4 Nuclear Spectroscopic Factors

Studying the secondary reactions of radioactive ion beams is presently of great interest in an attempt to understand and explain the nuclear structure and properties of short-lived exotic nuclei. For these kind of reaction studies, the single-particle structure of exotic nuclei is related to the measured experimental observables by nuclear many body theories. Observables such as one-nucleon removal cross section can be used to deduce the nucleon's single particle (sp) configuration ϕ_{ℓ_J} and spectroscopic factors for the specific states.

Typically, in a nucleon knockout reaction, the events are identified by the detection of the fragment of mass A-1 where A is the mass of the projectile. A single nucleon is removed from the projectile nucleus by a light absorptive nuclear target (in our case ^{9}Be). The schematic of a single nucleon knockout reaction is shown in the Figure 2.4 with a predicted momentum distribution of the fragment [Tos01].
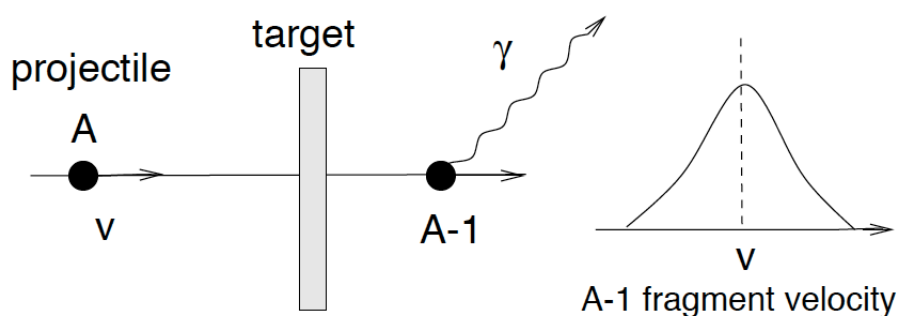
Figure 2.4: Schematic of a single nucleon knockout reaction with a predicted momentum distribution of the fragment. A de-excitation γ ray may or may not be emitted by the residual nucleus. Figure taken from [Tos01].

The fragment produced travels with a velocity very close to the velocity of the incoming projectile. The measurement becomes very inclusive when measuring only the heavy residue but not the removed nucleon. This results in larger cross section values which is very favorable in experimental point of view. A light nuclear target such as ^{9}Be behaves as a black absorptive disk to the incident core of the nucleons. When observed events survive near the beam energy, the charge-transfer interactions are highly peripheral with the result that the wave function of the removed nucleon will be explored far from the surface of the projectile. So the wave function will not be probed in the interior of the projectile providing strong surface localization. Figure 2.5 shows how a core fragment survive a collision when the reaction becomes peripheral, (that is, $b_c \geqslant R_c + R_t$). In this

way only that part of the wave function of the nucleon outside the core will be sampled [Tos01].
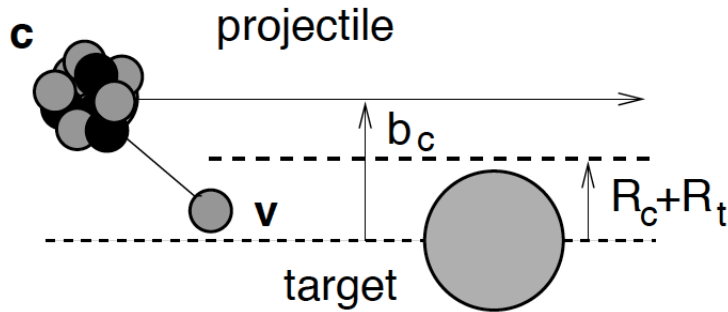
Figure 2.5: How a core fragment survive a collision when the reaction becomes peripheral, (that is, $b_c \geqslant R_c + R_t$). In this way only that part of the wave function of the nucleon outside the core will be sampled. Figure taken from [Tos01].

The total nucleon knockout cross section is the sum of two forms of cross sections (a) from stripping, thats is when the removed nucleon excites the target and is absorbed, and (b) from the elastic breakup of the projectile by leaving the target in its ground state. This latter process is called diffractive dissociation. The two processes produce distinct final states which are incoherent so the cross section from these two processes can be added without an issue.

The total cross-section can then be defined as

$$\sigma(c) = \sum C^2 S(c, \ell_j) \sigma_{sp}(S_n, \ell_j). \tag{2.2}$$

In this equation, C^2S is the spectroscopic factor of the single particle state of the nucleon with quantum number ℓ_j. This also indicates the origin of this single particle configuration in the many body wave function ϕ_A with respect to a specific core state c of the nucleons

remaining. The quantity σ_{sp} is the summed total nucleon knockout cross sections from both stripping and diffraction mechanisms for a nucleon with a S_n separation energy.

Single neutron knockout cross section of $^{24}O(0^+)$ to the ground state of ^{23}O and two neutron knockout cross section of ^{24}O could be described by adopting the eikonal model approach discussed herein. The nuclear reaction and structure parameters were chosen using the procedure described in detailed in Ref. [GAB$^+$08]. Equation 2.2 is transformed into Equation 2.3 when account for the theoretical partial cross-section for population of a given final state of the (A-1)-body residual nucleus (^{23}O) with j$^\pi$ spin parity and E^* excitation energy:

$$\sigma_{th} = \left(\frac{A}{A-1}\right)^N C^2 S(\ell j^\pi) \sigma_{sp}(n\ell j, S_n^*).$$ (2.3)

Here $(\frac{A}{A-1})^N$ is an A dependent center of mass correction term and N, the number of oscillator quanta of the major shell of the removed nucleon is equal to 2 ($N=2$) for the interested sd-shell orbitals here. Again, σ_{sp} is the single particle cross-section when the removed nucleon has quantum numbers $n\ell j$ and an effective separation energy of S_n^*. Here,

$$S_n^* = S_n(g.s) + E^*,$$ (2.4)

where $S_n(g.s)$ is the ground state separation energy of ^{24}O which is equal to 4.192 MeV according to the Ref. [MWP12], and E^* is the excitation energy which is 0 MeV for the $1/2^+$ state and 2.78 MeV for the $5/2^+$ state [EDA$^+$07, SFB$^+$07].

2.5 Rare Isotope Beam Production

At the National Superconducting Cyclotron Laboratory in Michigan the rare isotope beams are produced using the projectile fragmentation method [Mei12]. The process of producing rare isotopes occurs by fragmentation of the projectile nucleus at the target. The fragments are then sent away from the target in vacuum to be used in various experiments. Presently GANIL in France, RIKEN in Japan, and GSI in Germany also produce rare

isotope beams using the same projectile fragmentation method as the NSCL and provide beam time for numerous nuclear physics experiments using a variety of different rare isotopes produced.

An accelerated steady beam with an energy of 50 MeV/nucleon (140 MeV/nucleon ^{48}Ca in the present work), which is a higher energy than the Coulomb barrier, is reacted with a mass target. Projectile fragmentation takes place when the projectile nucleus which has a radius of R1 interacts tangentially by the impact parameter, b, with the target nucleus with radius R2. It is possible for some number of nucleons to be removed from the projectile, as shown in Figure 2.6 [Mei12]. After the reaction takes place the particle of interest is separated from other resulting reaction products and unreacted beam using the A1900 fragment separator, which consists of number of dipole and quadrupole magnets to select the desired element.
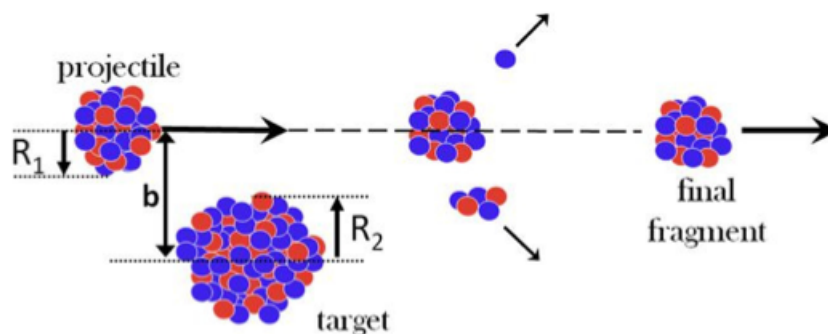
Figure 2.6: Reaction occurring in the projectile fragmentation method. Here, R1 and R2 are the radii of the projectile and target respectively. b is the impact parameter, which is the separation distance between the two nuclei [Mei12].

The type of the possible reaction that occur between the projectile and the target highly depends on the energy of the projectile beam and thus plays a major role in projectile fragmentation technique. In some energy regimes some specific reactions have higher

cross section values than other reactions. For an example in low energy regime, for energies lower than 20 MeV/nucleon, the projectile fragmentation process is hindered and elastic/inelastic scattering and compound nuclear reactions become prominent. In the energy regime of 20 MeV/nucleon to about 200 MeV/nucleon, the cross section for the projectile fragmentation is higher due to the high kinetic energy that is well above the Coulomb barrier. The energies higher than 200 MeV/nucleon are typically too large to allow for transfer or fusion reactions. In this case, chances are higher to have a "pure" fragmentation process due to the overlapping of the projectile and the target which makes it unable to produce a stable secondary beam [Mei12].

3   EXPERIMENTAL DETAILS

3.1   Experimental Facility

The experiment was conducted in the S3 vault of the National Superconducting Cyclotron Laboratory (NSCL) at Michigan State University using the high resolution S800 spectrograph shown in the Figure 3.1. The S800 is a type of a magnetic prism which is used to separate charged particles with different momenta. The large acceptances of the S800, both in solid angle and momentum, are well adjusted for the large emittance of secondary beams produced by projectile fragmentation. The charged particle detectors in the focal plane of S800 are useful for measuring the position and angle of the particles deflected by the magnetic field. Figure 3.1 shows two photographs of S800 spectrograph taken at the NSCL during the experiment.

Figure 3.1:   Focal plane detectors (left) and Superconducting Magnet (right) of the S800 spectrograph in the S3 vault at NSCL. Figure taken from [nsc].

3.2   Beam Production and Specific Experimental Details

In the experiment, a secondary beam of ^{24}O was produced with a 1% momentum spread using a primary beam of ^{48}Ca at 140 MeV/u and a Be production target with a thickness of 1551-mg/cm^2. Beryllium has very good thermal properties: because of the high melting point, it can withstand the high heat developed in the target due to the high energy deposited from the ^{48}Ca beam. The thicker the production target, the higher the intensity of the beam produced. On the other hand, too thick targets result in dispersing the secondary beam energy due to energy straggling and produce more unwanted particles as well. We used ^{48}Ca as the primary beam due to its very large neutron to proton ratio. A higher primary energy would give a higher secondary beam energy which in turn results in producing a forward kinematic boost for particles, however, 140 MeV/u is the maximum that the NSCL can produce and hence place a limitation to the energy of the primary beam. Although the maximum achievable momentum spread possible at the NSCL is 5% at the end of the A1900 fragment seperator, it is only 3% everywhere else. The momentum spread has been decreased to 1% using the momentum slits near the wedge in order to have a more defined beam energy, but consequently, this will also lower the intensity of the beam which indeed will be a disadvantage. LISE++ calculations were used to determine the rate of which ^{24}O will be produced at a 1% momentum acceptance [nsc].

After running the experiment in the ^{23}O setting to get the neutron knockout cross section to the ground state of ^{23}O with sufficient number of counts (about 4000 counts of ^{23}O), the S800 settings were changed to focus on ^{22}O in the remaining two days to measure the two neutron knockout cross section of ^{24}O.

Two timing scintillators were used at the focal plane of the A1900 and in front of the reaction target to measure the time of flight of the beam. Once the magnetic rigidity is known, the particles can be identified using the time-of-flight information. The energy of the ^{24}O beam was 92.3 MeV/u. The reaction of the neutron knockout occurred in a

188 mg/cm^2-thick Be reaction target. The LISE++ calculations predict a beam rate of 1.03 pps/pnA for ^{24}O at 1% momentum acceptance. By taking into account the 50% transmission loss through the beam line to the reaction target, the typical one neutron knockout cross section of about 10 mb uncertainty and the detection efficiency of the MoNA/sweeper setup which is about 56%, the count rate was calculated. The actual count rate during the experiment was

3.2.1 Coupled Cyclotron Facility

The NSCL uses samples of commonly used stable elements for experiments that use radioactive beams and vaporizes them at very high temperatures before removing away some of the outer layer electrons. Once they are ionized, the positive ions can then be handled by the electric and magnetic fields in the K500 and K1200 cyclotrons. Once the ions are injected to the K500 cyclotron, the magnetic field in there keeps the ions moving in a circular path while the internal electric field adds energy and thus speed to the ions in each circular motion. When these high-speed ions are transferred into the K1200 cyclotron, they get even more acceleration by the same technique. Once the particles move to the outer edges of the cyclotron due to the increased kinetic energy, they normally leave the cyclotrons and enter the beam line. Figure 3.2 shows the K500 and K1200 cyclotrons the NSCL uses to accelerate ions [XW99].
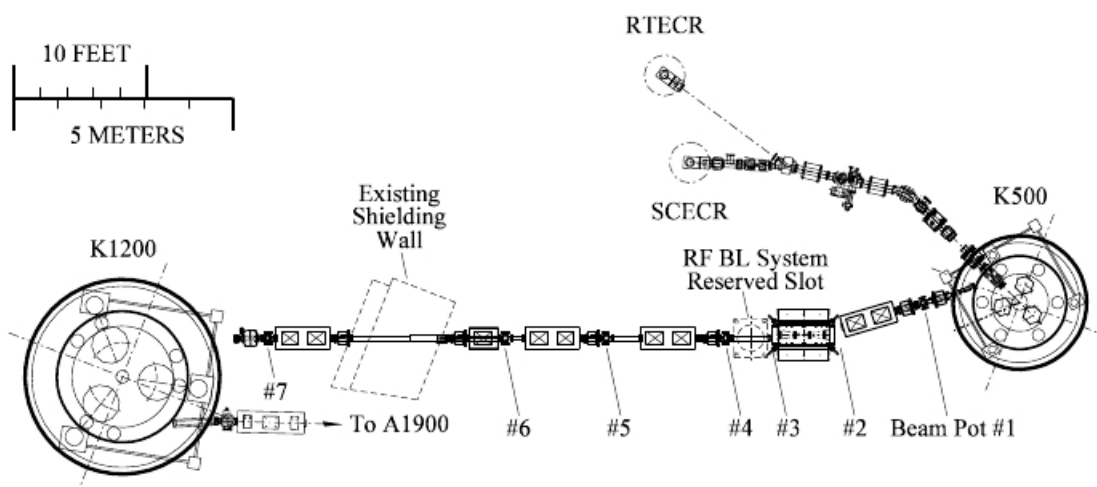
Figure 3.2: K500 and K1200 cyclotrons in the NSCL facility. The numbers through 1 to 7 indicate 7 beam diagnostic areas in which the beam intensity and profile are monitored using Faraday cups and phosphor screens. Figure taken from [XW99].

3.2.2   A1900 Fragment Separator

Although the secondary beam expected from the production target is ^{24}O, it includes many impurities. In order to improve the purity, the A1900 fragment separator was used with an achromatic Al degrader (the wedge) of 1050 mg/cm^2 thickness placed in the middle of it at the intermediate image (shown in Figure 3.3) along with a 14 mm slits at the focal plane.
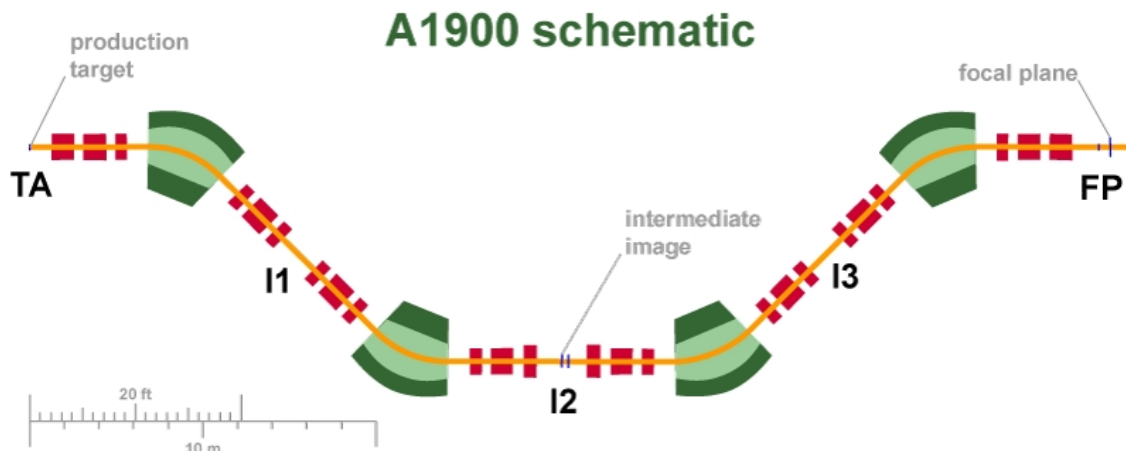
Figure 3.3: A1900 Fragment Separator used to clean out and improve the purity of the secondary beam. The green "wedges" represent the 4 dipole magnets while the red boxes represent the 24 quadrupole magnets. Figure taken from [nsc].

The dipole magnets are used to separate secondary beam particles produced by the production target before the A1900 depending on their magnetic rigidities. The first set of two dipole magnets (D1 and D2) are set for choosing particles with a specific magnetic rigidity. The particles with different rigidities than this specific value are removed by sweeping them away to the sides, so they will not present in the beam line. The Aluminum wedge type degrader is placed in the mid position of the A1900 to further purify the beam. The beam enters the A1900 has a wide momentum distribution thus a wide range of B-rho values. The particles with higher momenta bends more while low momentum particles bend less. The high rigidity particles will reach the thicker part of the wedge and lose more energy when passing through whereas particles with lower momentum will reach the thinner part of the wedge and lose much less energy. In the degrader, different particles will lose energy differently, so they exit from the degrader with different magnetic rigidities and a fairly narrow momentum distribution. When this beam goes through the other two dipole magnets (D3 and D4), the beam gets filtered further and thus it is possible to obtain a very pure secondary beam of ^{24}O. The energy of the ^{24}O beam was 92.3 MeV/u corresponding

to a magnetic rigidity of 4.17 Tm of the D1 and D2 magnets and 4.00 Tm in D3 and D4. The A1900 fragment separator also consists of 24 superconducting quadrupole magnets to focus the beam and to check the beam in between [nsc].

3.3   The S800 Spectrograph

The S800 is a type of a magnetic prism which can deflect and separate charged particles with different momenta. The high resolution ($\Delta E/E = \times 10^{-4}$ with a nominal 1 mm diameter beam spot at the object position) and the large acceptance (5%) allow us to distinguish particles with only slightly different energies and identify large number of particles after they react with the thick Be target. The detectors of the S800 measure the position and angle of the particles deflected by the magnetic field. Figure 3.4 shows a schematic of the S800 spectrograph at the NSCL [nsc].

The S800 has a QQDD configuration (two quadrupole magnets and two C-type dipole magnets). Having one strongly focussed y quad just after the target and an x-focussed quad before the dipoles allows a large solid angle (20 msr), and a good efficiency, respectively. The maximum rigidity (deflection by the magnetic field) is 4 Tm with a momentum spread of 5%. This rigidity is sufficient for typical experiments which use beam energies less than 100 MeV/u (800 MeV for protons) [DB03]. There is an energy loss through the target. So if we know the energy loss from the Barney plots (the information sheets containing magnet settings, currents rigidities, and energies of the beam at different moments of the experiments) and the target thickness is known, it is possible to find the correct rigidity value (momentum/charge). For higher beam energies, there are various methods to reduce the secondary beam energy to be appropriate for S800. However, they all will result in some degree of intensity loss. In the first half of the experiment where the focus was on ^{23}O, the S800 was set to a B-rho value of 3.9 Tm. It was set to 3.7278 Tm for the ^{22}O in the

second half of the experiment. The ^{24}O unreacted particles are steered though the magnets by setting the B-rho value to 4.0925 Tm.
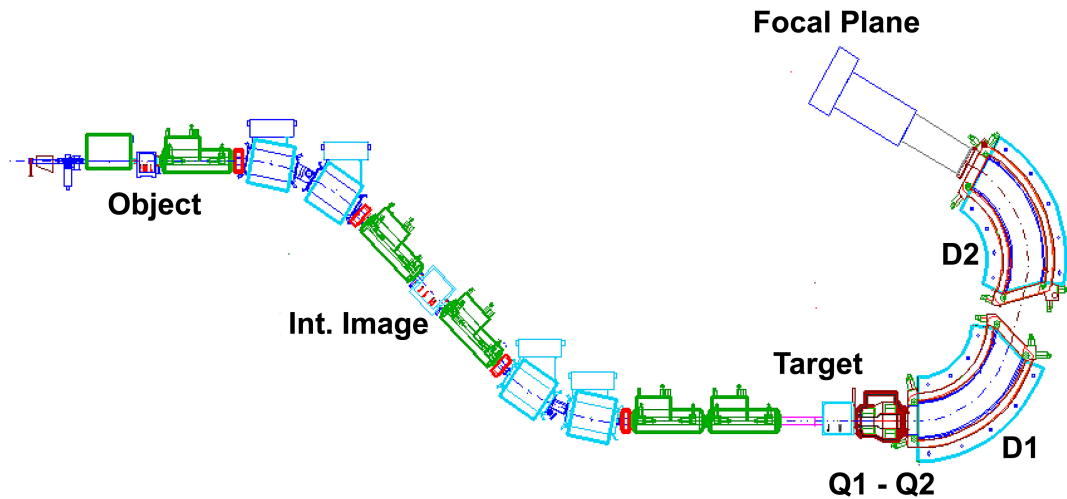
Figure 3.4: Components of the S800 Spectrograph at NSCL. Figure taken from [nsc].

The ion optical design of the spectrometer is fixed and is consist of two main parts. The analysis line is considered to be the part from the place the beam enters into the spectrometer to the place the Q1 is situated. The rest is considered as the high acceptance spectrograph itself (see Figure 3.5). The functionality of the analysis line proceeds by different optical modes, namely focussing and dispersion matching. Focussing and dispersion matching is done using the quadrupole magnets and dipole magnets in the analysis line. In the S800 spectrograph, only focussing mode is used. In focus mode, we focus the beam such that the position and angle do not depend on y position of the target. The beam is focussed so that there is no first order dependance on the dispersive direction (y direction) [DB03].

When the charged particles go through the magnetic field generated by the dipole magnets (D1 and D2), the direction of the moving particle's trajectory is altered. The magnitude of this deflection depends on the specific mass-to-charge ratio of each particle. This works according to the Lorentz equation and Newtons law for a centripetal force which is radially inwards,

$$F = qVB = \frac{mv^2}{R} \tag{3.1}$$

and thus the particle travel in a curve with a radius of curvature R. The dipole magnets create a homogeneous magnetic field over the distance and by placing several dipole magnets in the beam line can increase the bending power of the system. Quadrupole magnets are used for particle beam focussing. When the quadrupole magnets are in hyperbolic shape, due to the constant magnetic field gradient is generates, they can act as a focussing lens in either the x or y direction. When placing two x focussing and y focussing quadrupole magnets consecutively but not adjointly, they can be used to achieve a good focussing of the beam along both x and y axis.

3.3.1 Beam Line Components

The components in the S800 beam line are used to monitor and to calibrate the secondary beam by using specific information such as time of flight details. There is a timing scintillator called the extended focal plane (XFP) just after the A1900 fragment separator. Approximately 30 m away from the XFP, there is another fast timing scintillator naming the object scintillator which is located just before the S800 magnets. This timing scintillator is mainly used for time of flight information and as well as for the evaluation of beam intensity and transmission efficiency. Figure 3.5 shows a schematic of the beam line [nsc].
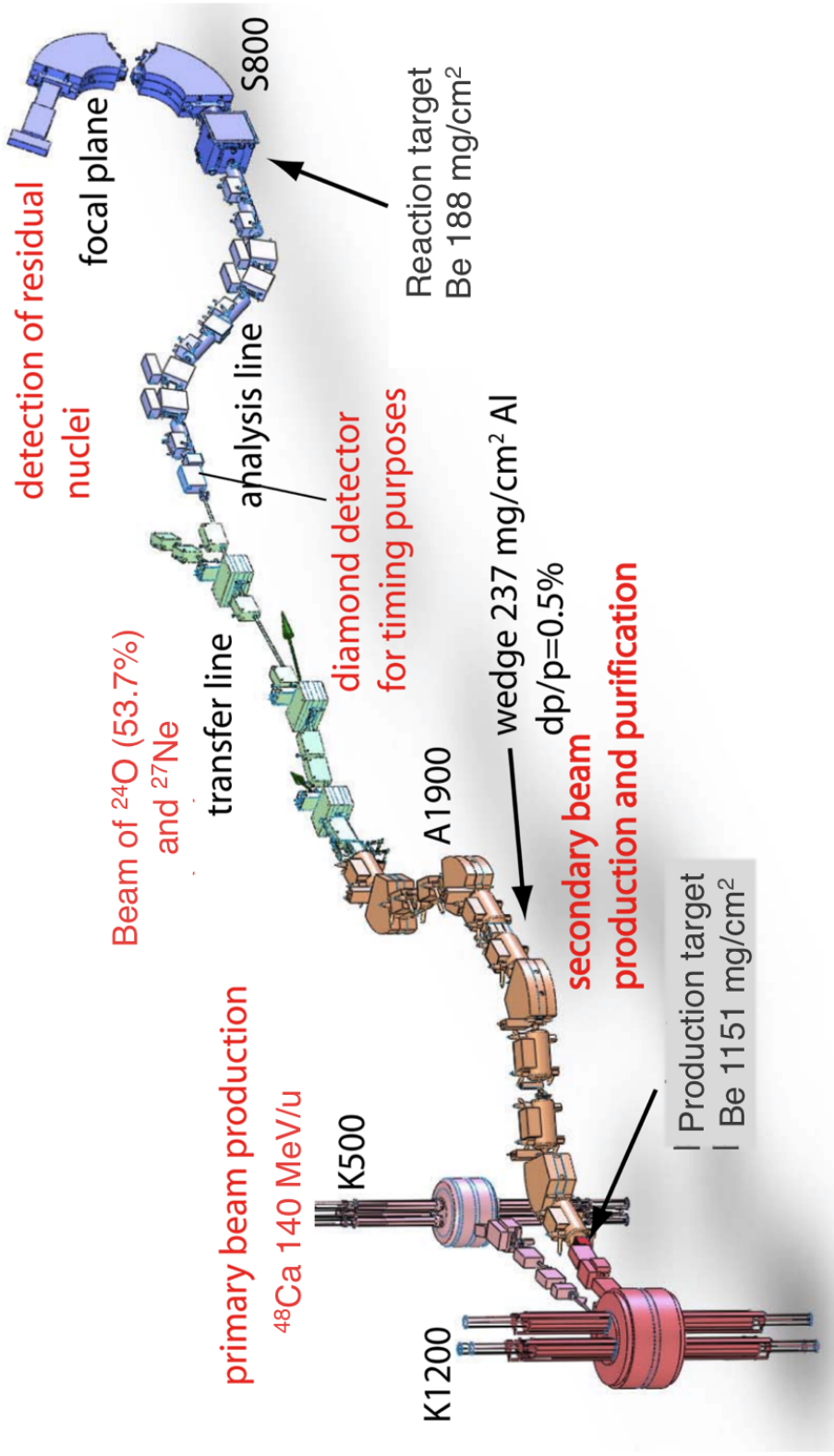
Figure 3.5: A schematic of the beam line going from the couple cyclotron facility to the S800 focal plane via A1900 fragment separator. Figure was initially taken from [nsc] and adapted to the current experiment.

3.3.2   Spectrograph and its Focal Plane Detectors

The focal plane of the S800 spectrograph is equipped with two cathode readout drift chambers (CRDC), an ionization chamber, a thin scintillator and a hodoscope. The CRDCs are used to measure the x and y position of the beam while the Ion chamber and the thin scintillator are used for energy loss measurements. The two PMTs of the thin scintillator is also used to measure the time of flight of the particles. The beam loses all its energy at the hodoscope and come to a rest. Figure 3.6 shows how these detectors are placed inside the vacuum chamber of the S800 focal plane [Mei12].
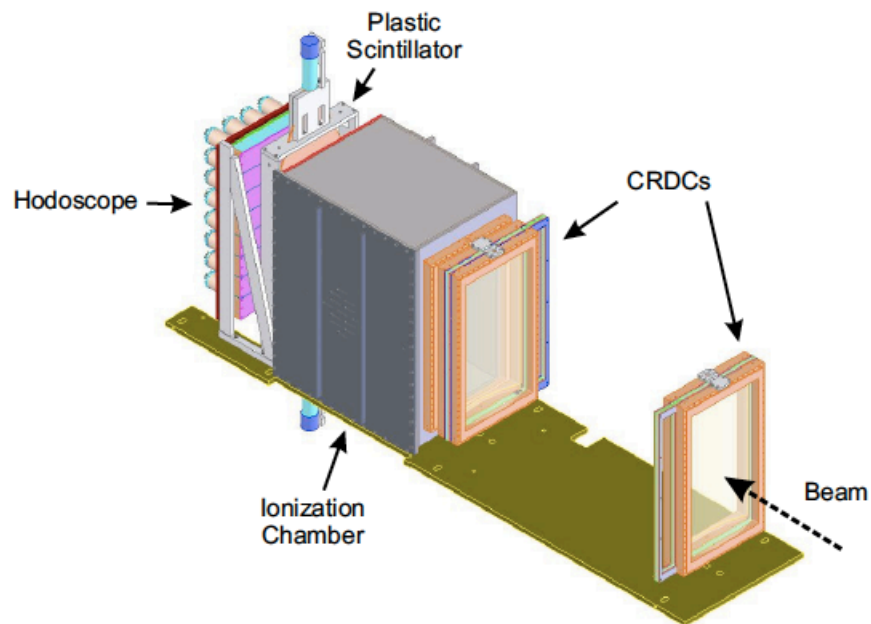
Figure 3.6: A schematic of The Ion chamber, Thin Scintillator and the Hodoscope placed inside the vacuum chamber of the S800 focal plane. Figure taken from [Mei12].

3.3.2.1 Cathode Readout Drift Chamber [crd]

Cathode readout drift chamber (CRDC) is used to measure the position and the angle of the charged particles. In this experiment we use two CRDC detectors approximately 1m apart from each other. The CRDC detector is followed by a plastic scintillator to provide a reference time to measure the drift time of the electrons inside the CRDCs. The CRDCs have a position resolution of 0.5 mm in both directions [crd].
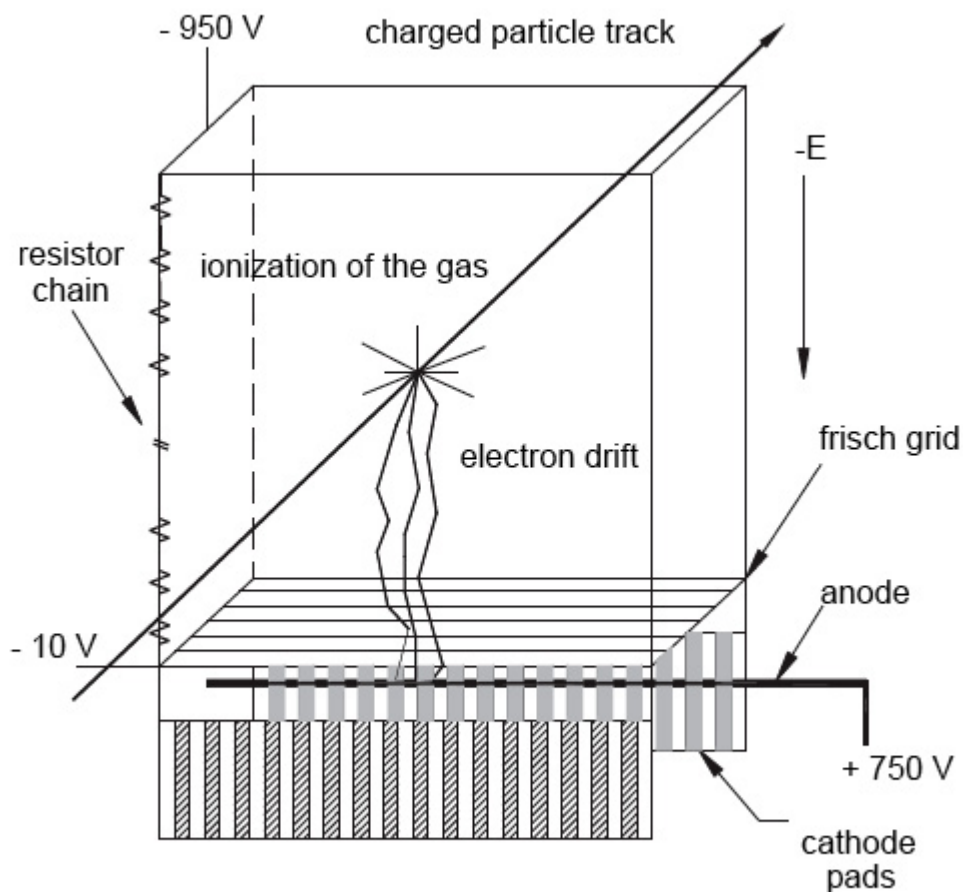
Figure 3.7: A drawing of a Cathode readout drift chamber. Figure taken from [Fra06].

The gas filled inside the CRDC is a mixture consisting of 20% Isobutane (C_4H_{10}) and 80% Tetrafluoromethane (CF_4) at an operating pressure of 50 Torr. When the pressure is lowered than this, then there can be gas discharge (sparking) and gas becomes conductive and as a result the current increases. So the voltage will be tripped and stay at zero volts because it is unable to produce that large current. The lower limit of the pressure is 50 Torr to obtain a maximum drift voltage without experiencing sparking. Also 50 Torr is the maximum pressure the 12 m windows of the CRDCs can safely take. This pressure is within the functioning range of the detectors. If we wanted to run at higher pressure, we would have to increase to thickness of the windows, which would in turn increase multiple scattering and decrease the angular resolution (which is around 2 mrad). As shown in Figure 3.7 [Fra06] the uppermost part of the CRDC, the chamber, is filled with the above mentioned gas and is connected with a plate of -950 V of voltage. At the end of this region, there is a Frisch grid which operates at a voltage of -10 V. Down stream, there is a positively charged anode wire held at 750 V. The gas mixture inside the chamber allows the beam particles to go through the gas and to ionize the gas molecules by removing electrons and thus produce charged pairs without creating an electron avalanche effect. The upper part of the CRDC has a homogeneous voltage and the lower part has a cylindrical-symmetry voltage. This is due to the fact that in the upper region we don't need the avalanche effect to take place but we need it in the lower part to have more electrons to generate a good signal. The charged pairs produced in the gas are separated by using the voltage difference between the highly negatively charged plate above and the Frisch grid. Therefore the electrons liberated from the ionization pass through the gas towards the Frisch grid whereas the positively charged ions move towards the plate. The drift velocity particles attains due to this drift voltage is measured to provide timing information. The electrons passed through the Frisch grid are collected in the anode wire held at 750 V. In order to increase the number of electrons there is a small avalanche effect in the region near the anode wire. Each CRDC

consists a switched capacitor arrays (SCA) and an analog to digital converter (ADC) and a total of 224 channels (Cathode pads) in them. After the electrons were collected in the anode wire, it induce a charge on each 224 cathode pads which will eventually be used to determine the x position of the particles by studying the distribution of charges along the pads. The y position can be obtained by using the drift time measurements determined by the timing difference between trigger and anode wire signal. The changes done to the anode wire voltage and thus to the electric field between gas molecules and anode wire can have potential effects on the signals. During the migration of the charges to the anode and cathode, many collisions normally occur with neutral gas molecules and consequently increasing the gas multiplication effect which will be potentially affect the charge signals [crd].

A proportional counter is a detector where we have gas multiplication. The upper part of the CRDC acts as an ion chamber and lower part acts as a proportional counter. The pressure of the lower part of the CRDC is set so that it produce more holes and electron pairs and thus get larger signals in the proportional counter. There will be a negative current pulse in the anode wire due to the charge collection and this can induce a charge in the pads which depends on the time. Each pad is coupled with capacitors which are connected to a switch. The charge can flow through the connection and once the capacitor connects with the pads, the charge will flow through the capacitor and can be detected by digitizing the capacitor signal.

3.3.2.2 Ionization Chamber

The ionization chamber is the second charged-particle detector in the S800 spectrograph and it is located after the CRDC2 in the beam line. Particles lose energy inside the P-10 gas (90% argon and 10% methane) filled ion chamber which is operating at 150 Torr air pressure. The anodes inside the ionization chamber are divided into 16 pads and are at-

tached to a positive voltage of 100 V. When the charged particles pass through the filled gas of the Ion Chamber, electrons generated from the disassociation of charged pairs are pulled towards the Frisch grid due to the voltage difference between the highly negatively charged upper plate and the Frisch grid. Then charge is accumulated in the 16 pads (channels). This overall charge collection directly gives an idea of how much energy was lost inside the chamber by the charged particles. Combined signal from all 16 pads gives the total energy loss during the time. Signals from the ionization chamber helps for both secondary beam particle identification and isotope identification. Since the ion chamber usually has 100% detection efficiency, it is used as a reference to measure the detection efficiencies of other charged particle detectors inside the S800 spectrograph and timing detectors in the beam line.

3.3.2.3   Scintillator Detectors

The thin Scintillator is the last detector in the charged particle detector series in the focal plane of S800 which is used for particle identification. Thin scintillators are mainly used to find the energy of the beam as well as the timing information. The time of flight measurements obtained from the thin scintillator used in this experiment are used to do isotope identification after doing the time of flight corrections and gain matching. For the energy information, we need to calibrate the gain of the individual photo multiplier tubes (there are two for each detector). Because the gain is different, the energy signal in the PMT is not the same. We must correct the individual tubes with respect to one another. The time taken to reach each PMT should be the same. We obtain separate energy signals and timing signals for each PMTs of thin scintillator. The timing information is quite important as it tells us the position where the beam hits on the detector. In the S800 experiments the thin scintillator is followed by a hodoscope which is used to make the particles fully stopped

by losing all of their energies however, the hodoscope measurements were not used in this experiment to calculate the cross section.

4 DETECTOR CALIBRATION AND ANALYSIS

A sorting program called RAWSORT was written using Fortran to read raw hex data stored during the experiment and write them into ntuples. Some detector calibrations have also been included in this RAWSORT program such as obtaining CRDC positions in mm. The N-Tuples made by the RAWSORT program are converted into Root files and the remaining detector calibrations, particle identifications, and corrections are done using the Root graphical analyzing tool while all the energy loss and kinematic factors were calculated using the LISE++ program.

The experimental goal of the e07031 experiment was to determine the neutron knockout cross section of ^{24}O to the ground state of ^{23}O which is neutron bound. Therefore the analysis of this experiment involves the S800 spectrometer but does not include MoNA. After calibrating all the charged particle detectors in the S800, the analysis of the data of e07031 experiment was performed.

4.1 Secondary Beam Particle Identification

As mentioned in Sec. 3.2, the secondary beam particle of interest ^{24}O was produced by a ^{48}Ca beam using a Be production target. Before the A1900 fragment separator, the beam included ^{27}Ne, ^{25}F, ^{26}F and ^{22}N along with ^{24}O so the A1900 dipoles and quadruples were set to purify the beam. However, due to the close momentum/charge values that ^{24}O and ^{27}Ne possess, both presented in the beam at the end of the A1900 fragment separator. The measured rate at the A1900 focal plane was 0.54 pps/pnA (particles per second per nano Amps) and the purity at ±5 mm focal plane gap was 42%. The measured rate for ^{24}O at S800 focal plane was 0.25 pps/pnA with a purity of 46%.

The time of flight spectrum of the secondary beam before the reaction target was obtained by calibrating the times of the XFP timing detector at the exit of the A1900 and object timing scintillator just before the reaction target. The magnetic rigidity and the

energy of the two major particles were calculated using the LISE++ program along with their velocities, 12.5122 cm/ns and 13.633 cm/ns for ^{24}O and ^{27}Ne, respectively. This information together with the distance between the two timing detectors in cm was utilized to do the time calibrations in ns. The two particles were clearly separated from other peaks and a gate was placed around ^{24}O peak before calibrating any other detector to get the isotope identification. Figure 4.20 shows the time of flight spectrum from XFP (A1900) to object scintillator (in front of the reaction target) for a run with unreacted beam setting (unreacted ^{24}O). Figure 4.2 is the same time of flight drawn with the partially calibrated (in arbitrary units) energy loss through the Ion Chamber.
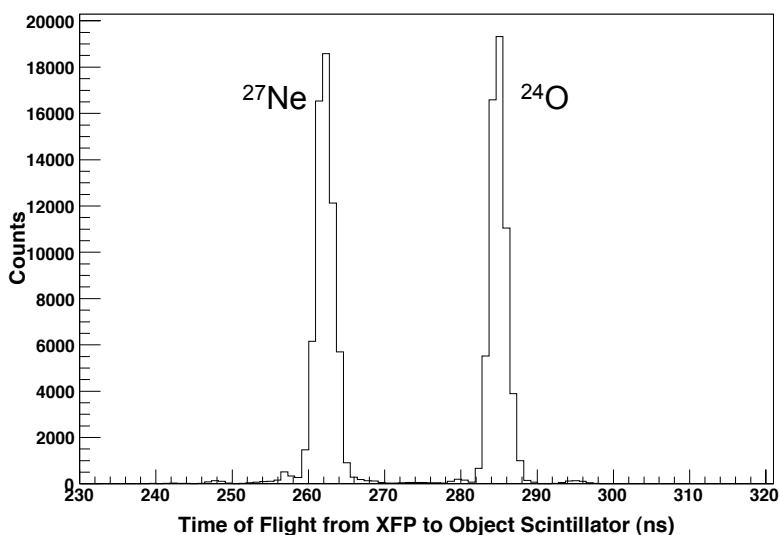
Figure 4.1: The calibrated time of flight spectrum from A1900 (XFP) to object scintillator (in front of the reaction target), for an unreacted run.
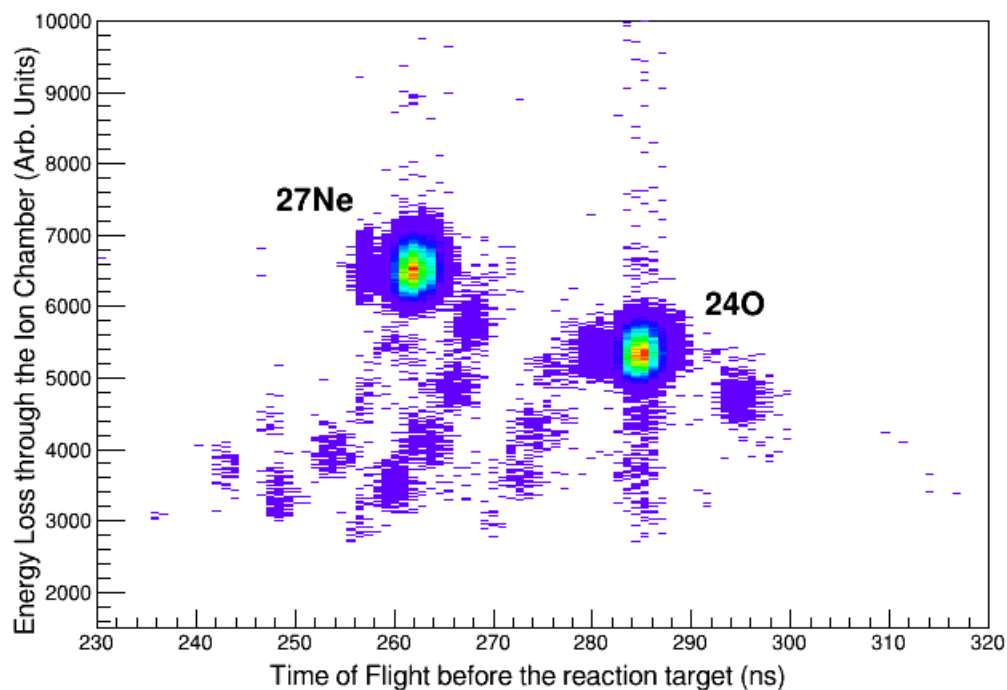
Figure 4.2: Total Ion Chamber energy loss versus the calibrated time of flight spectrum from A1900 (XFP) to object scintillator (in front of the reaction target), for an unreacted run.

4.2 Detector Calibrations

4.2.1 CRDC Calibration

Each pad of the CRDC has a different gain and thus interprets charge in a different manner. In order to give all the pads the same amplification we calculated a shift and a gain for each pad and applied it. In order to find the gain and shift we needed to calculate the pad average. Starting from an initial shift and gain obtained from pedestal values we found new shift and gain for the charges accumulated in all 224 channels using a Paw program. The new gain and new shift calculated were taken as temporary values and iterated many times until the newer new shift and gain are 0 and 1 respectively. Figure 4.3 shows a raw spectrum of charge distribution of CRDC 1 of experiment e07031 and the gain-matched

spectrum of the same detector using the final gain and shift values found. Figure 4.4 shows the final gain and shift values we used for this gain matching process. For the first and last 75 pads, gains and shifts were chosen to be 1 and 0 respectively due to the very low charge accumulations in those pads. That means those pads are not gain matched.
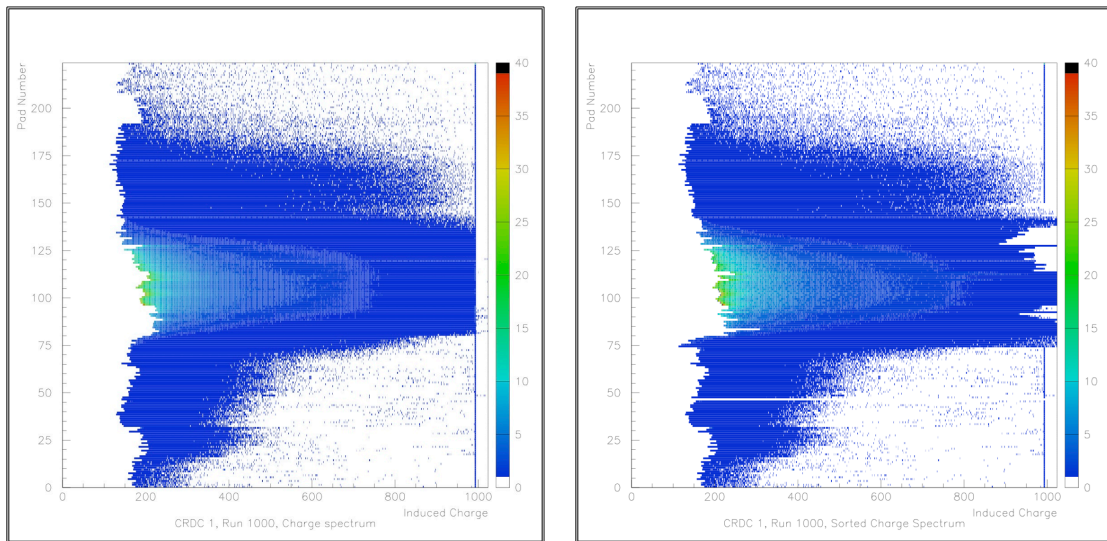
Figure 4.3: Raw (left) and gain-matched (right) CRDC 1 charge spectra.
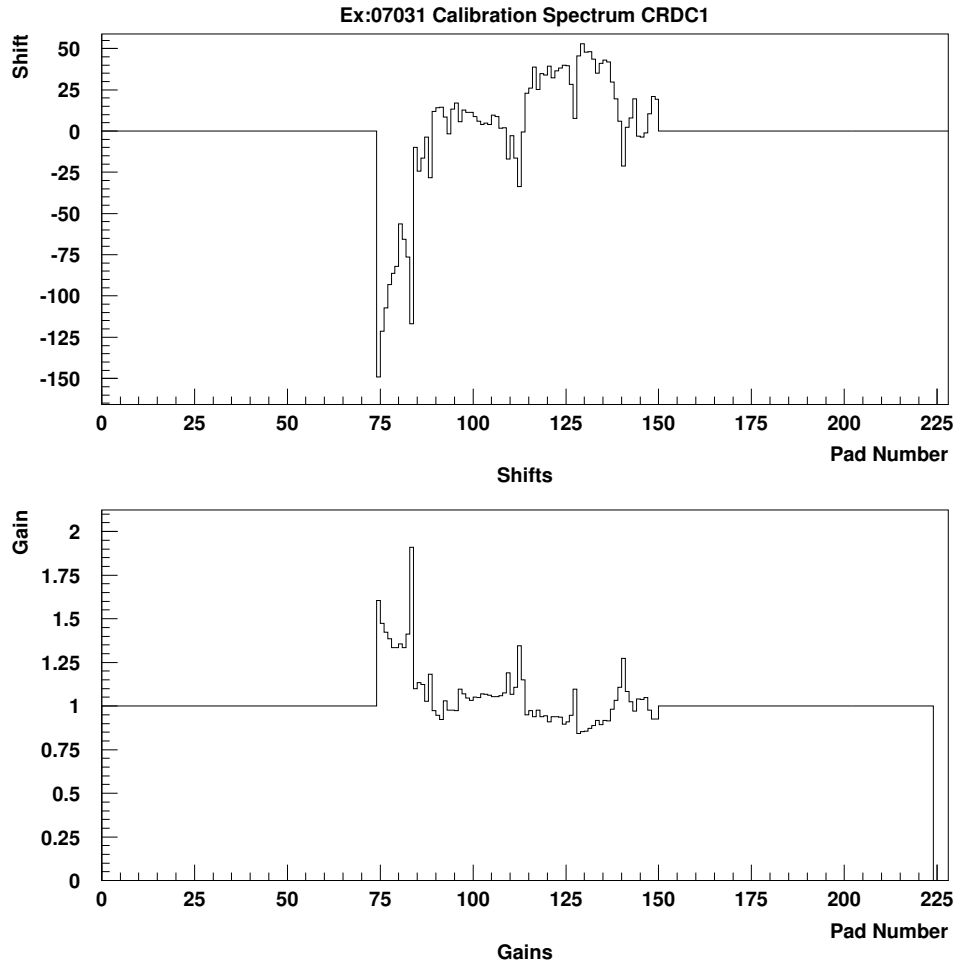
Figure 4.4: Final gain and shift values used for the gain matching process.

Both *x* and *y* positions are required to obtain the angle at the focal plane to do the reconstruction of the beam trajectory. To get the *y* position a de-focused beam was sent through a mask placed in front of each CRDC. The hole pattern of each CRDC1 and CRDC2 masks are different from one another and *x* and *y* positions of each CRDC detector are mirrored with the holes in their specific mask. The positions and the spacing of each hole in the mask are known and are then used to calibrate the detectors. The pad pitch of 2.54 mm was used to determine the dispersive plane position (*x* position) of CRDC

however the mask runs were utilized for verification purposes. Figure 4.5 shows the charge spectrum of the mask run for CRDC2 detector. The calibrated *x* and *y* positions of CRDC1 in mm are shown is Figure 4.6.
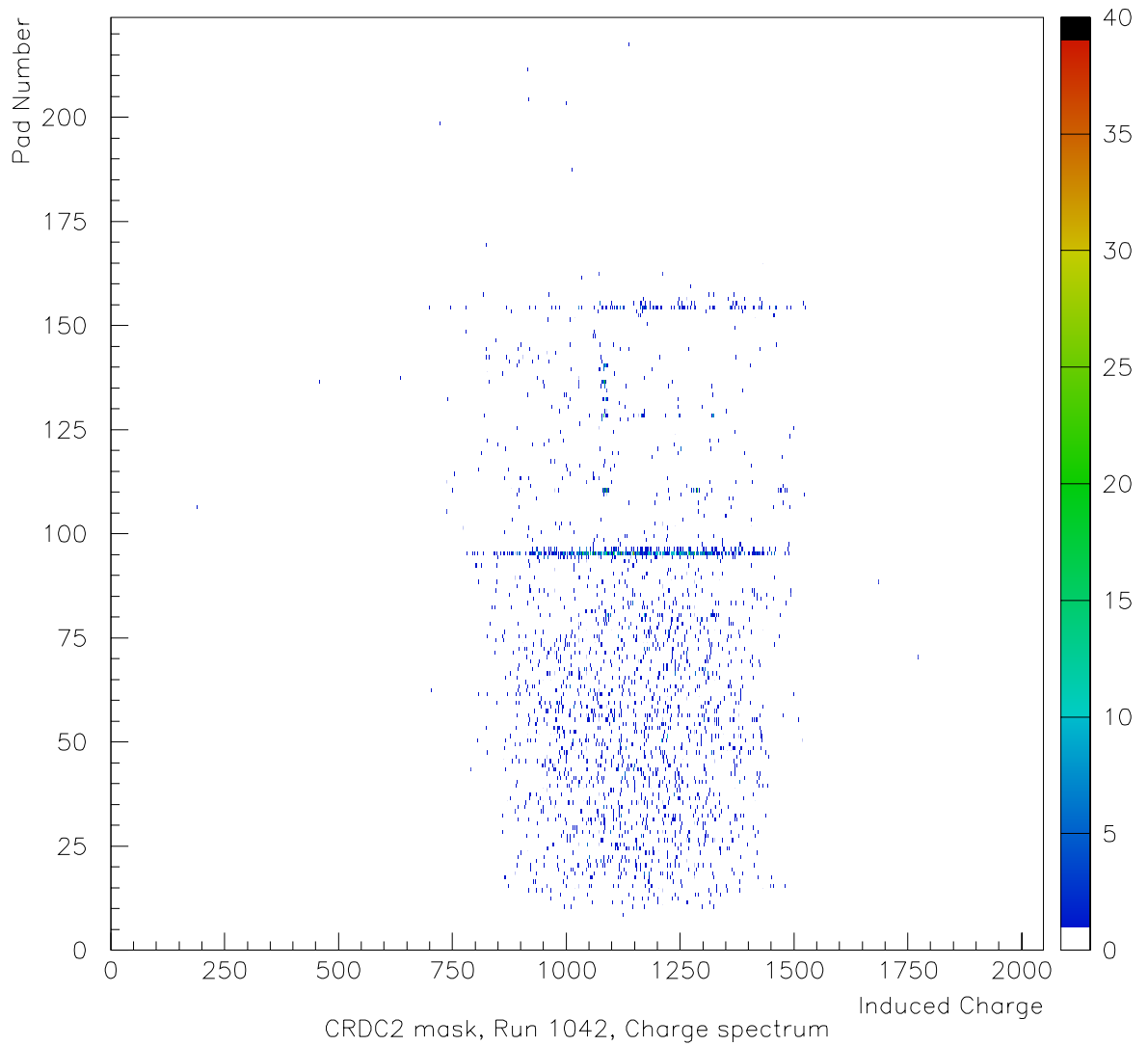
Figure 4.5: Charged spectrum of the mask run for CRDC2.
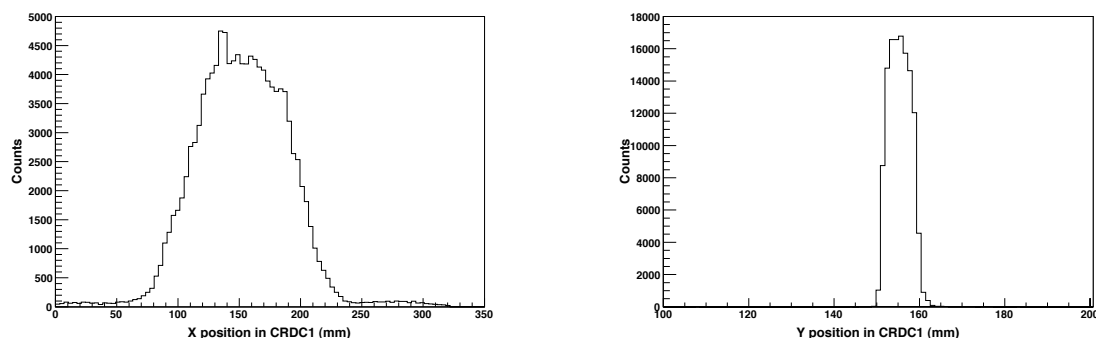
Figure 4.6: The *x* (left) and *y* (right) positions of CRDC1 in mm for an unreacted run.

4.2.2   Ion Chamber Calibration

The Ion Chamber was gain matched by taking the energy of each pad with respect to the pad number 8. The first and the last pads were not included when obtaining the total energy loss through the ion chamber due to the incomplete charge collection at the edges. After the pads are gain matched, the ion chamber energy should be as much as possible position independent for proper particle identification. The total ion chamber energy was not depending on the CRDC *x* and *y* positions so there was no need for a correction. Figure 4.7 shows the Ion chamber energy in pad 8 versus the energy in pad 2, and equations 4.1, 4.2, 4.3 and 4.4 show how the total energy was obtained by normalizing the energies of each pad from pad 2 to pad 15. The energies from pad 1 and pad 16 were not taken into account due to their incomplete charge accumulation. Figures 4.8 and 4.9 show the total ion chamber energy drawn with the CRDC *x* and *y* positions respectively.
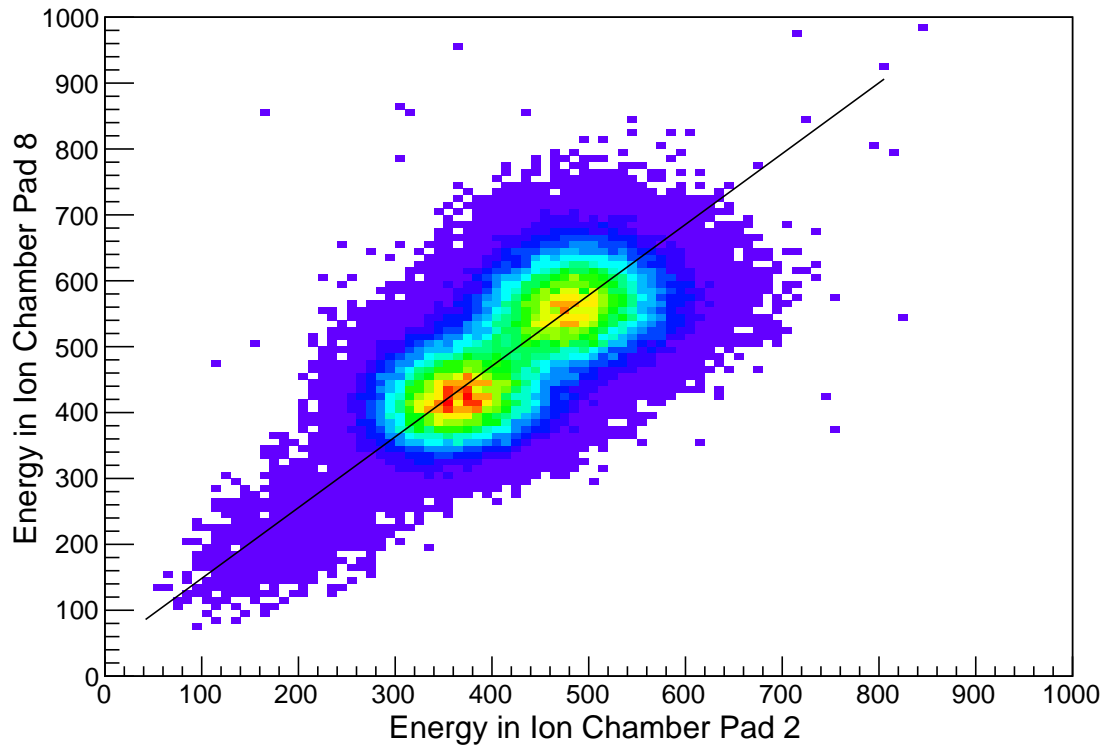
Figure 4.7: Ion Chamber energy (in arbitrary units) in pad 8 versus pad 2.

$$IC_{pi}(N) = a_i + b_i IC_{pi} \tag{4.1}$$

where $2 \leqslant i \leqslant 15$ and i represent the pad number. The normalization parameters a and b are different for each pad from pad 2 to pad 16.

$$IC_{tot} = \sum_{i=2}^{15} IC_{pi}(N) \tag{4.2}$$
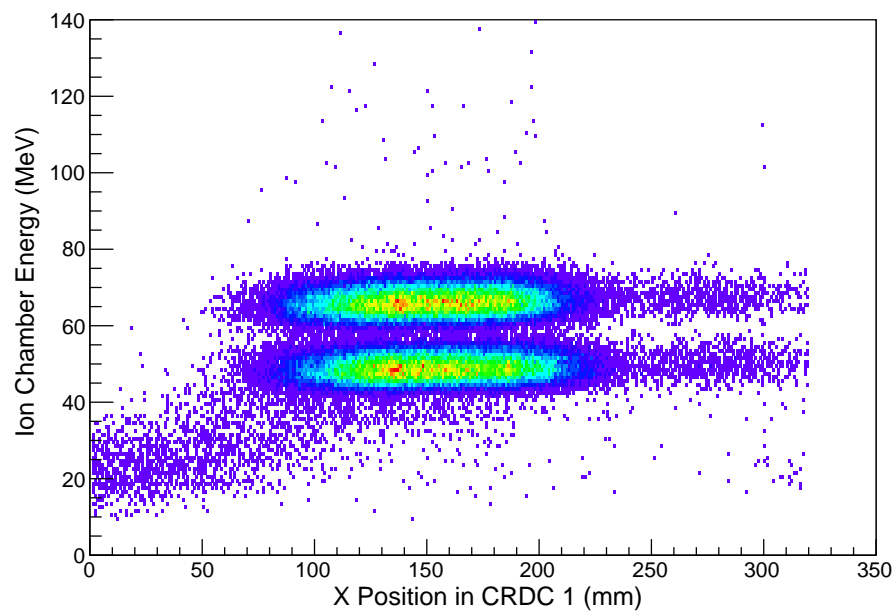
Figure 4.8: Total Ion Chamber energy versus CRDC *x* position.
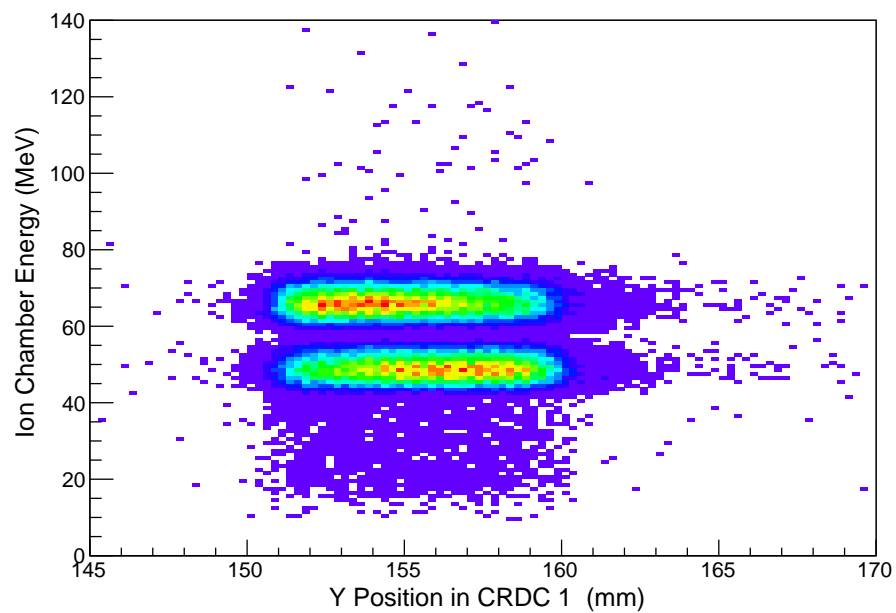
Figure 4.9: Total Ion Chamber energy versus CRDC *y* position.

4.2.3   Thin Scintillator Calibration

The thin scintillators are mainly used to determine the energy and timing information of the beam. However, we obtain separate energy signals and timing signals for each PMT of thin scintillators. The timing information is quite important as it tells us the position where the beam hits on the detector, as well as the time of flight between it and the timing scintillator near the reaction target, which is used in isotope identification. The two x and y positions of the beam on the thin scintillator were found by extrapolating the x and y positions of CRDC1 and CRDC2 by using the distance between CRDC1, CRDC2, and the thin scintillator in the s800 focal plane. Figure 4.10 shows the x and y positions where the beam hits the thin scintillator.
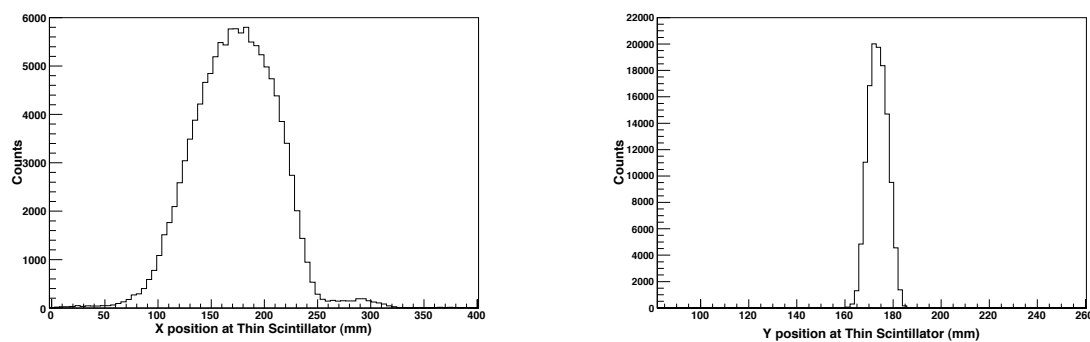
Figure 4.10:   Thin scintillator x (left) and y (right) positions in mm for an unreacted run.

The PMT raw energy signals should be independent of the position thus were corrected to get a fairly straight spectrum with respect to the thin scintillator positions. The energies were first corrected for the x position and then corrected for the y. The total corrected energy was obtained by obtaining the geometric mean of all the PMT signals. Figures

4.11 and 4.12 show the energy of the thin scintillator PMT1 versus thin scintillator *x* and *y*

position while Figures 4.13 and 4.14 show the position-corrected PMT1 energy. The total

corrected averaged energy of the two PMTs are shown in Figure 4.15.
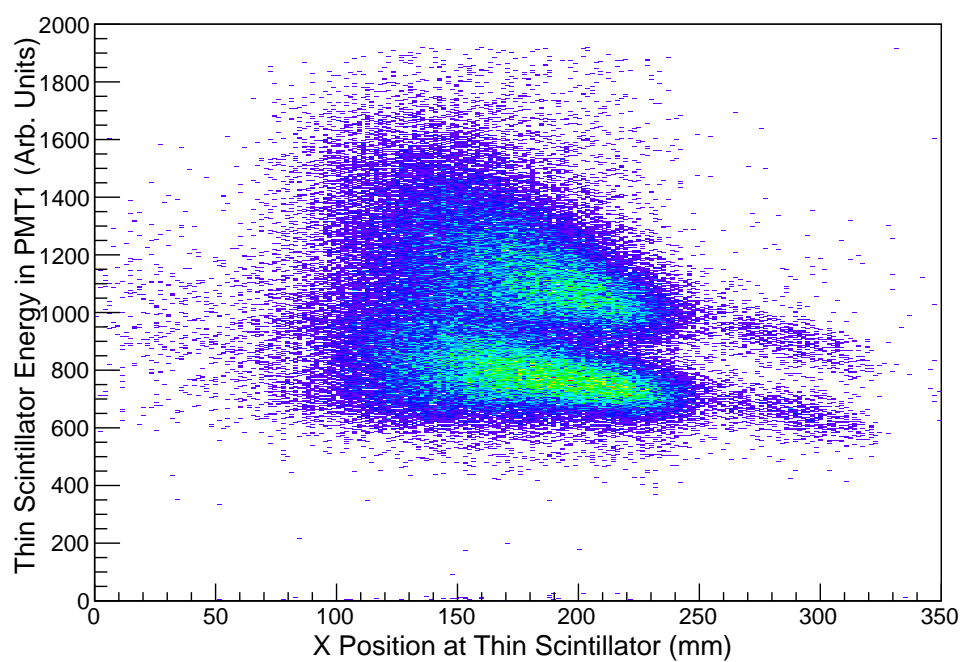
Figure 4.11: Uncorrected thin Scintillator PMT1 energy (in arbitrary units) versus *x* position for an unreacted run.
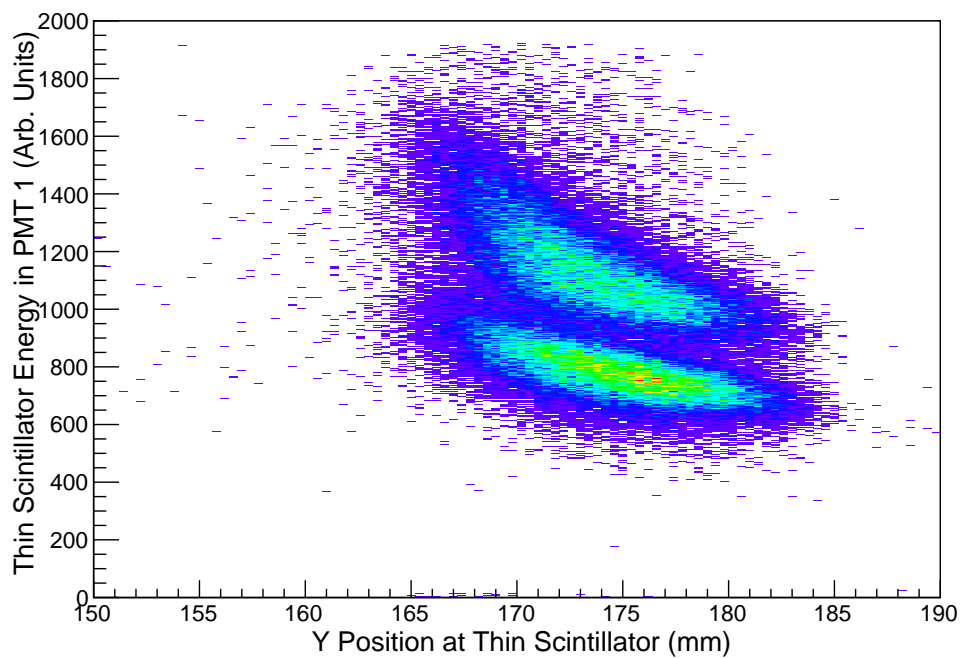
Figure 4.12:   Uncorrected thin Scintillator PMT1 energy (in arbitrary units) versus *y* position for an unreacted run.
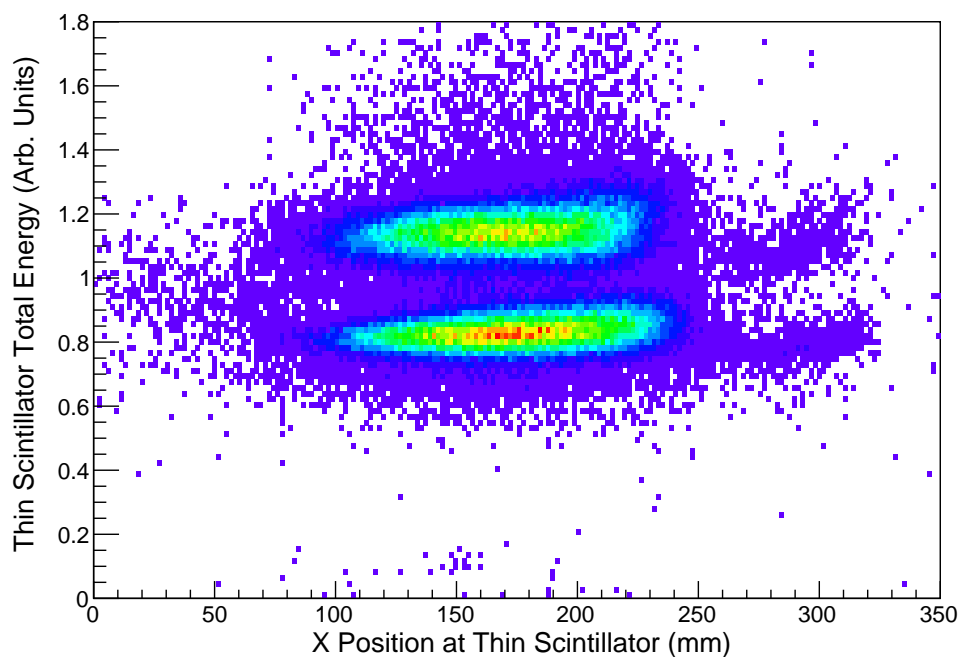
Figure 4.13:   Position-corrected total thin scintillator energy loss versus *x* position for the same unreacted run used to produce Figs 4.11 and 4.12.
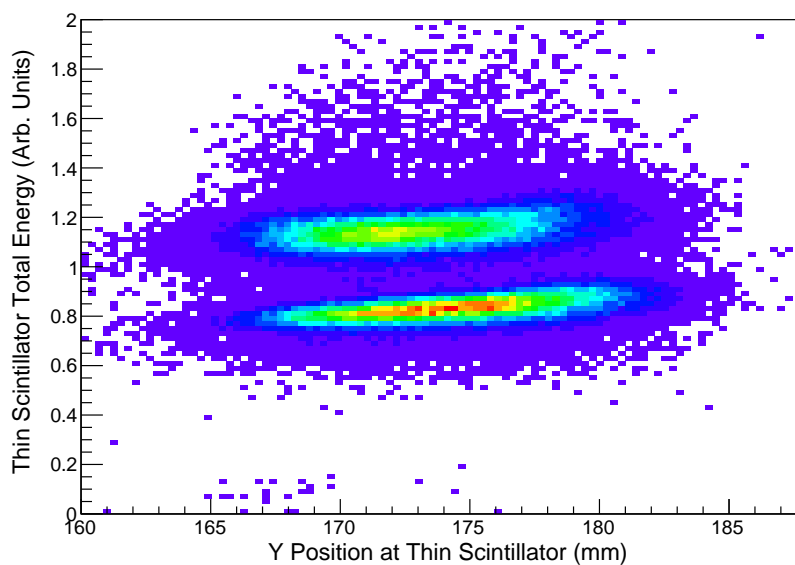
Figure 4.14: Position-corrected total thin scintillator energy loss versus *y* position for the same run used to produce Figs 4.11 and 4.12.
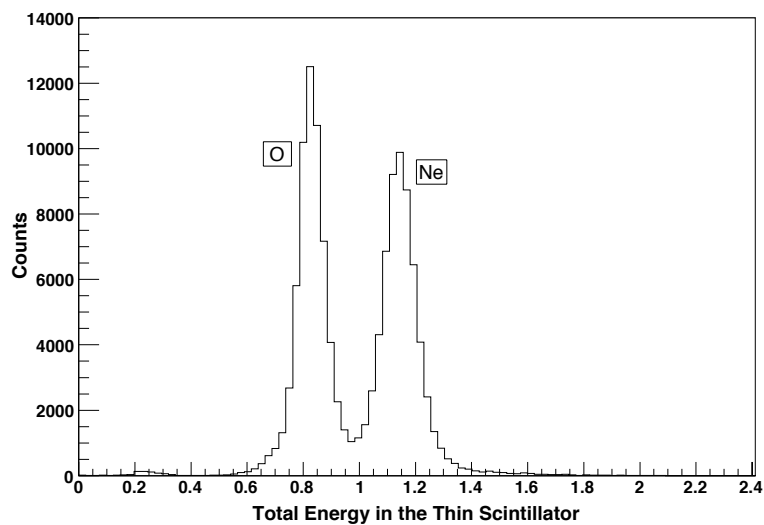
Figure 4.15: Counts versus total corrected and averaged thin scintillator energy.

4.3   Time of Flight Corrections

The time of flight spectrum of charged fragments was calculated using the timing signal from the object scintillator just before the reaction target and the averaged timing signal from the two PMTs of thin scintillator detector. After the beam enters the thin scintillator it takes time to travel inside the scintillator plastic to reach to each PMT. We need to correct this in order to get the absolute timing information from the two PMTs. The time the beam takes to travel to each PMT inside the scintillator is,

$$d_i = \left[(t_x - x_i)^2 + (t_y - y_i)^2\right]^{1/2} \tag{4.3}$$

where (t_x, t_y) are the positions calculated at the dE thin scintillator that are projecting from CRDC 1 and 2. The index i represents each PMT with positions of (x_i, y_i) of (0,275), (0,-275) (in mm) for the upper PMT, and the down PMT respectively [2]. The x and y positions at the thin scintillator are defined as,

$$t_x = 1.378(x_{2mm} - x_{1mm}) + x_{1mm}, \tag{4.4}$$

and

$$t_y = 1.378(y_{2mm} - y_{1mm}) + y_{1mm}, \tag{4.5}$$

respectively, where x_{1mm}, x_{2mm}, y_{1mm} and y_{2mm} are the positions of CRDC 1 and 2 in mm. The d_1 and d_2 for the first and second PMT respectively are,

$$d_1 = ((t_x)^2 + (t_y - 275)^2)^{1/2}, \tag{4.6}$$

and

$$d_2 = ((t_x)^2 + (t_y + 275)^2)^{1/2}, \tag{4.7}$$

where d_1 and d_2 represent the distances to PMT 1 and 2 (respectively) from the impact position on the thin scintillator. With d_1, d_2, speed of light c, and the index of refraction 1.58 [2] through the scintillator plastic, t^*_1 and t^*_2 give the time it takes for the light to go from the particle impact position on the thin scintillator to each PMT defined as,

$$t^*_1 = \frac{1.58 d_1}{c}, \tag{4.8}$$

and

$$t^*_2 = \frac{1.58 d_2}{c} \tag{4.9}$$

This time was subtracted from the calibrated timing signal from each PMT, and then averaged to get the final absolute timing information. The quantities t_1 and t_2 are the timing signals measured in thin scintillator before calibrating with the magnetic trigger timing trg. The multiplication of the calibrated timing signal by 0.1 is to convert the time into the units of ns. The T_1 and T_2 then provide the absolute corrected timing information of the beam as showing in the equations,

$$T_1 = [(t_1 - trg)(-0.1)] - t^*_1, \tag{4.10}$$

and

$$T_2 = [(t_2 - trg)(-0.1)] - t^*_2. \tag{4.11}$$

The absolute time from the two PMTs are averaged to get the time as shown in,

$$T_{avg} = (T_1 + T_2)/2. \tag{4.12}$$

4.4 Isotope Identification

The oxygen isotope identification was done using the time of flight spectrum from object scintillator (in front of the reaction target) to the thin scintillator of the combined production runs using the corrected timing information after placing a gate in the ^{24}O peak

in the A1900 (XFP) to object scintillator time of flight spectrum. Figure 4.16 shows the time of flight spectrum from the object scintillator to the thin scintillator in the S800 focal plane for a combination of production runs from run1001 to run1039 . Figure 4.17 shows the same spectrum plotted with the total calibrated ion chamber energy loss. The same plot after applying the ^{24}O gate found in the XFP to object scintillator time of flight spectrum is shown in the Figure 4.18.
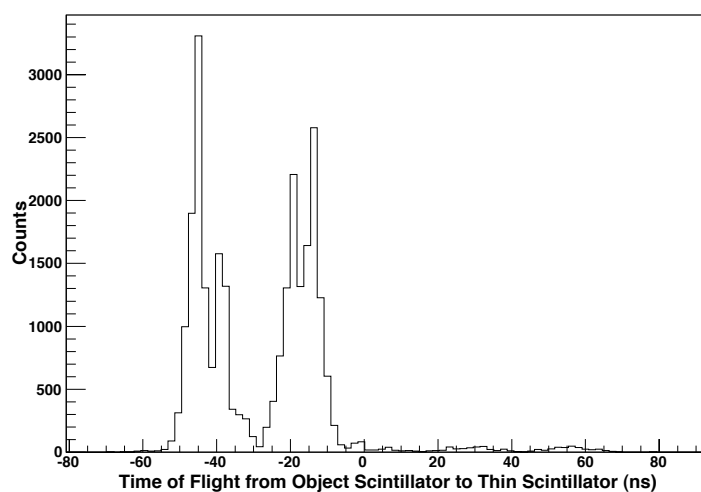
Figure 4.16: Time of flight spectrum from the object scintillator (in front of the reaction target) to the thin scintillator for combined production runs.
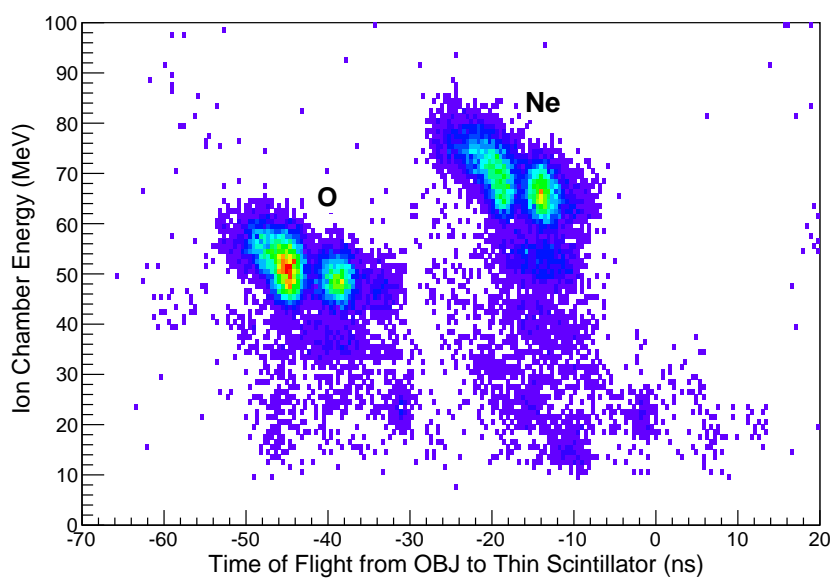
Figure 4.17: Total ion chamber energy versus time of flight spectrum from the object scintillator (in front of the reaction target) to the thin scintillator for combined production runs.
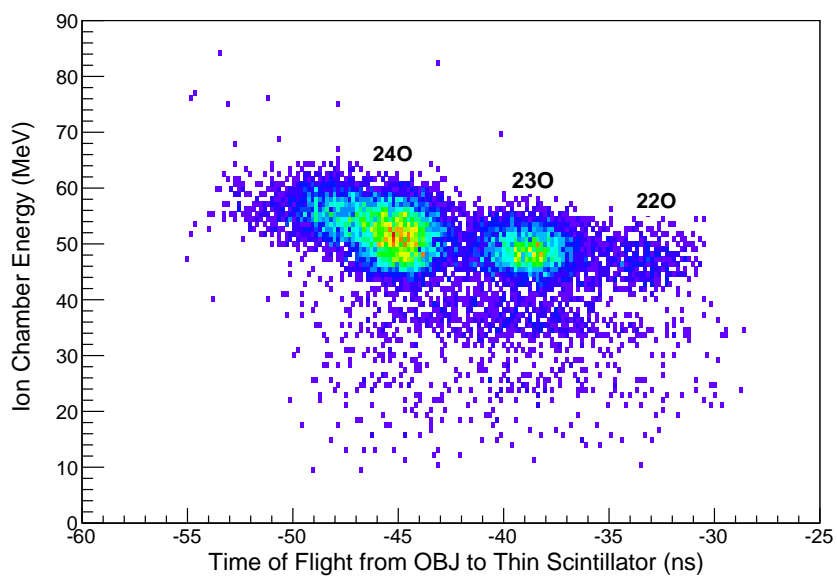
Figure 4.18: Total ion chamber energy versus time of flight spectrum from the object scintillator to the thin scintillator after applying the ^{24}O gate for combined production runs.

4.5   Cross Section Calculation

The purpose of the experiment was to measure the neutron knockout cross section from the ground state of ^{24}O to the ground state of ^{23}O. However while the first half of the experiment was focused on this purpose, the S800 settings were changed in the final two days to focus on ^{22}O to obtain the two neutron knockout cross section of ^{24}O. The cross sections in millibarns were calculated separately for the two scenarios using the appropriate experimental information.

4.5.1   Neutron Knockout Cross Section to the Ground State of ^{23}O

The cross section calculation was done using both unreacted runs for the determination of the number of incoming ^{24}O particles and Production runs for the number of reacted ^{23}O particles. The scalers in each detectors taken during the experiment for each run were also used in the calculation. Target thickness in mb^{-1} was used with its uncertainty to obtain the final cross section. The thickness of the target, 188 mg/cm^2, was converted into units of mb^{-1} with the result 1.26×10^{-5} mb^{-1}. Following is an explanation to show how the calculation was done. Table 4.1 shows the quantities and corresponding symbols used in the equations in the explanation.

Table 4.1: Quantities used in the equations for the cross section calculations and the correspondent symbols used.

Quantity	Symbol
Cross Section	σ
Target Thickness	t
Number of detected particles	N_d
Number of beam particles	N_b
Particles per scaler count	P
Scalers in the Object Scintillator	C_{obj}
Live time correction	τ
Efficiency correction	ϵ
Counts in the ^{23}O peak	^{23}O
Counts in the ^{24}O peak	^{24}O

The number of detected particles N_d and beam particles N_b are related through the cross section σ, and target thickness t as shown in,

$$N_d = \sigma N_b t. \tag{4.13}$$

The number of detected particles comes from the counts under the ^{23}O peak in the final time of flight spectrum showed in Figure 4.19. The number of beam particles is coming from the object scintillator scaler value (counts in the object scintillator) which is given by,

$$C_{obj} = \frac{N_b}{P} \tag{4.14}$$
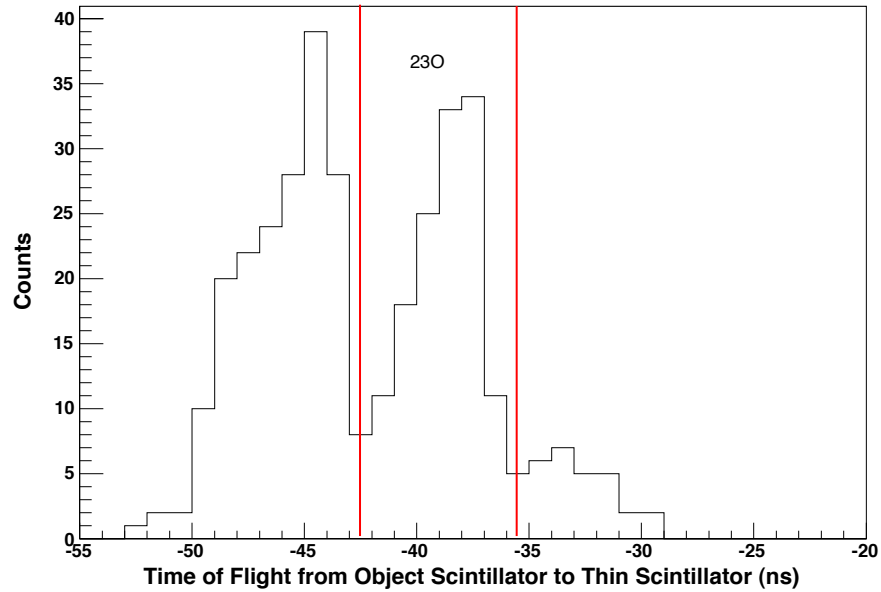
Figure 4.19:   The calibrated time of flight spectrum from Object Scintillator to the thin scintillator of a single production run (Run1009).

The Neutron Knockout cross section times the target thickness is then given by,

$$\sigma t = \frac{N_d}{N_b} = \frac{^{23}O}{C_{obj}P\tau\epsilon},$$

(4.15)

and the cross-section is,

$$\sigma = \frac{^{23}O}{C_{obj}Pt\tau\epsilon}.$$

(4.16)

The live time correction (τ) was included in the calculation to account for the differences the actual number of triggered events that occurred and the ones written to disk. The ratio between the live trigger scalers and raw trigger scalers (which was averaged around 0.96) would give this ratio as shown in,

$$\tau = \frac{\eta_{Live\,Trg}}{\eta_{Raw\,Trg}}.$$

(4.17)

The efficiency ϵ of the object scintillator has also taken into account to obtain the actual number of particles that enter the detector, not only the ones that were detected. The efficiencies were 99.99% for the CRDCs and scintillators.

The particles per scaler count was obtained from the unreacted runs using the number of particles under the ^{24}O peak in the XFP to object scintillator time of flight spectrum along with specific OBJ scalers. The spectra are shown in Figure 4.20.
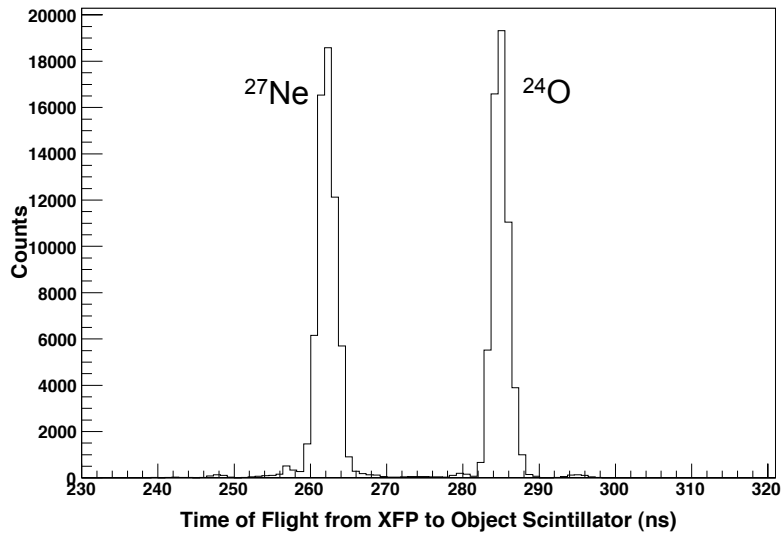
Figure 4.20: The calibrated time of flight spectrum from A1900 (XFP) to object scintillator in an unreacted run.

For the unreacted runs, the detected particle rate is equal to the incident particle rate. Thus,

$$^{24}O = C_{obj}P\tau\epsilon \tag{4.18}$$

$$P = \frac{^{24}O}{C_{obj}\tau\epsilon}. \tag{4.19}$$

There were two unreacted runs for the first production setting (^{23}O) and one for the second setting of ^{22}O. The first unreacted run, number 1000, was utilized to find the particles per scaler count which was then used for the cross section calculation using the production runs 1001 to 1013. The one found from the unreacted run, number 1017, was used for the production run number 1018 to 1039.

Table 4.2 shows the calculation of the particles per scaler count using equation 4.19 for the three unreacted runs. Note that the efficiency of the object scintillator and the scintillator at the extended focal plane (near A1900) is 99.99% for the runs 1000 and 1017 whereas it is 100% for the run number 1040.

Table 4.2: Parameters used for the calculation of Particles per scaler count.

Run Number	Live Trigger	Raw Trigger	OBJ Scalers	^{24}O Particles	Particles/ scaler count
1000	142328	147273	152496	124123	0.8423
1017	35087	36683	38125	30841	0.8458
1040	58692	61326	66900	53500	0.8412

Table 4.3 shows the counts in the object scintillator, number of ^{23}O particles, and specific particles per scaler count for all the production runs used to calculate the neutron knockout cross section of ^{24}O to the ground state of ^{23}O. Also shown are the number of incident particles which is the multiplication of the object scintillator counts and particles per scaler count. The dead time correction factor which was 0.12% (the value of the τ being 0.9988 on average for all the production runs) for all the production runs was negligibly small compared to the statistical error and thus was ignored for the cross section calculation.

Table 4.3: Parameters used for the calculation of one neutron knockout cross section of ^{24}O to the ground state of ^{23}O.

Run Number	OBJ Scalers	^{23}O Particles	Particles per scaler count	^{23}O/Incident counts ($\times 10^{-5}$)	Statistical Error ($\times 10^{-5}$)
1001	217534	122	0.8423	66.6	6.0
1002	224334	123	0.8423	65.1	5.9
1003	219534	92	0.8423	49.8	5.2
1004	177878	87	0.8423	58.1	6.2
1005	215415	111	0.8423	61.2	5.8
1006	199412	88	0.8423	52.4	5.6
1007	145203	64	0.8423	52.3	6.5
1008	172482	118	0.8423	81.2	7.5
1009	252742	138	0.8423	64.8	5.5
1011	244994	150	0.8423	72.7	5.9
1012	259988	149	0.8423	68.0	5.6
1013	230984	140	0.8423	72.0	6.1
1018	242663	152	0.8458	74.1	6.0
1019	237276	121	0.8458	60.3	5.5
1020	230441	137	0.8458	70.3	6.0
1021	205613	122	0.8458	70.2	6.4
1025	259691	163	0.8458	74.2	5.8
1026	272270	167	0.8458	72.5	5.6
1027	216115	136	0.8458	74.4	6.4
1028	208058	122	0.8458	69.3	6.3
1029	217109	133	0.8458	72.4	6.3
1030	195004	134	0.8458	81.2	7.0
1031	176287	92	0.8458	61.7	6.4
1032	189100	125	0.8458	78.2	7.0
1033	191441	122	0.8458	75.3	6.8
1034	131718	76	0.8458	68.2	7.8
1035	162179	105	0.8458	76.5	7.5
1036	110874	71	0.8458	75.7	9.0
1037	251412	135	0.8458	63.5	5.5
1038	245770	134	0.8458	64.5	5.6
1039	120986	57	0.8458	55.7	7.4
Total		3730			

Figure 4.21 shows the ratio between number of ^{23}O particles and incident ^{24}O particles with statistical uncertainties for all the production runs used in this cross section calculation and their error weighted average. The χ^2 of the distribution was calculated to be approximately 1.7. The ^{23}O particle number or the number of incident ^{24}O particles do not include the background elimination.
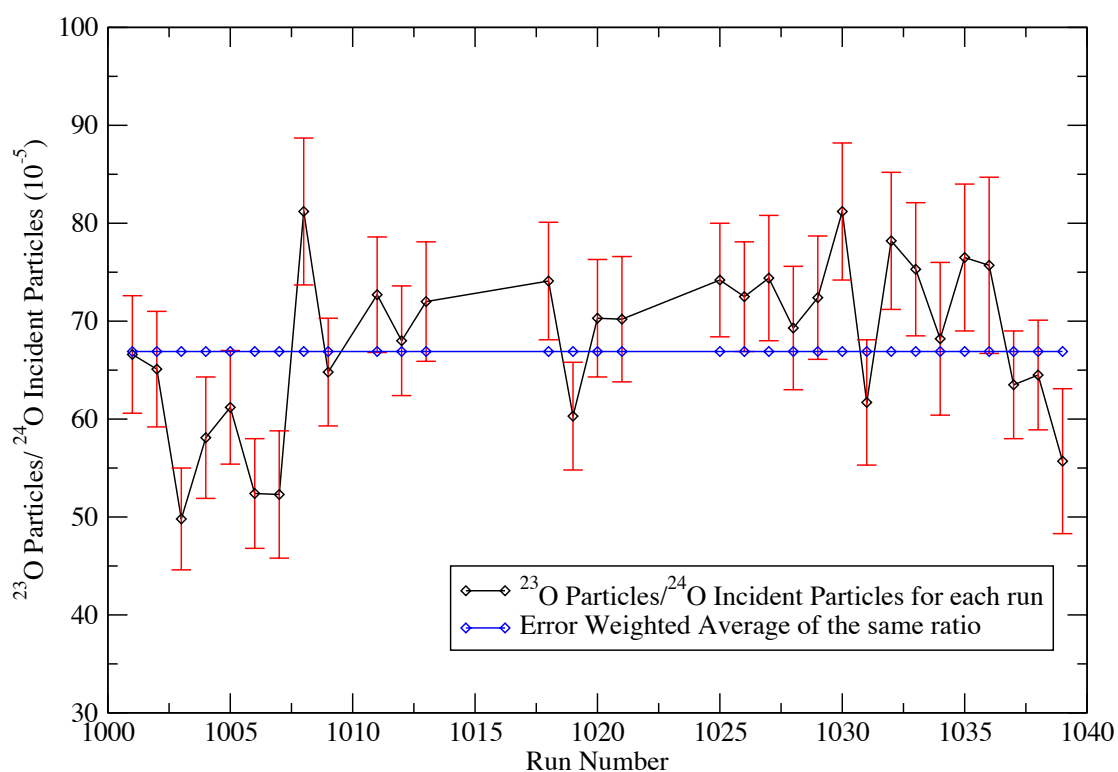
Figure 4.21: The ratio between number of ^{23}O particles and incident ^{24}O particles with statistical uncertainties for all the production runs used in the cross section calculation. The solid flat line represents the error weighted average of the ratio for all those runs.

4.5.2 Two Neutron Knockout Cross Section of ^{24}O

There were 17 production runs in the second half of the experiment which was dedicated for the ^{22}O setting. Just like above, the incident particle numbers were calculated for each of these runs by using the OBJ scintillator counts and the particles per scaler count value found from the final (number 1040) unreacted run. These parameters are tabulated in Table 4.4. Again the dead time correction was ignored and the efficiencies were taken to be 100%.

Table 4.4: Parameters used for the cross section calculations

Run Number	OBJ Scalers	^{22}O Particles	Particles per Scaler Count	^{22}O/Incident Particles ($\times 10^{-5}$)	Stat. Error ($\times 10^{-5}$)
1043	283002	279	0.8412	117.2	7.0
1044	278840	321	0.8412	136.9	7.6
1045	265525	270	0.8412	120.9	7.4
1046	247955	219	0.8412	105.0	7.1
1047	227131	229	0.8412	119.9	7.9
1048	240572	224	0.8412	110.7	7.4
1049	258218	232	0.8412	106.8	7.0
1050	275502	251	0.8412	108.3	6.8
1051	252742	245	0.8412	115.2	7.4
1052	218047	224	0.8412	122.1	8.2
1053	227167	247	0.8412	129.3	8.2
1054	285732	274	0.8412	114.0	6.9
1055	114112	112	0.8412	116.7	11.0
1056	315358	349	0.8412	131.6	7.0
1057	327364	356	0.8412	129.3	6.9
1058	496593	512	0.8412	122.6	5.4
1059	467267	468	0.8412	119.1	5.5
Total		4812			

Figure 4.22 is comparison of the ratio between the number of ^{22}O particles and incident ^{24}O particles with statistical uncertainties for all the production runs used in this cross section calculation and their error weighted average. The χ^2 of the distribution was calculated to be 1.4. The ^{22}O particle number or the number of incident ^{24}O particles do not include the background elimination.
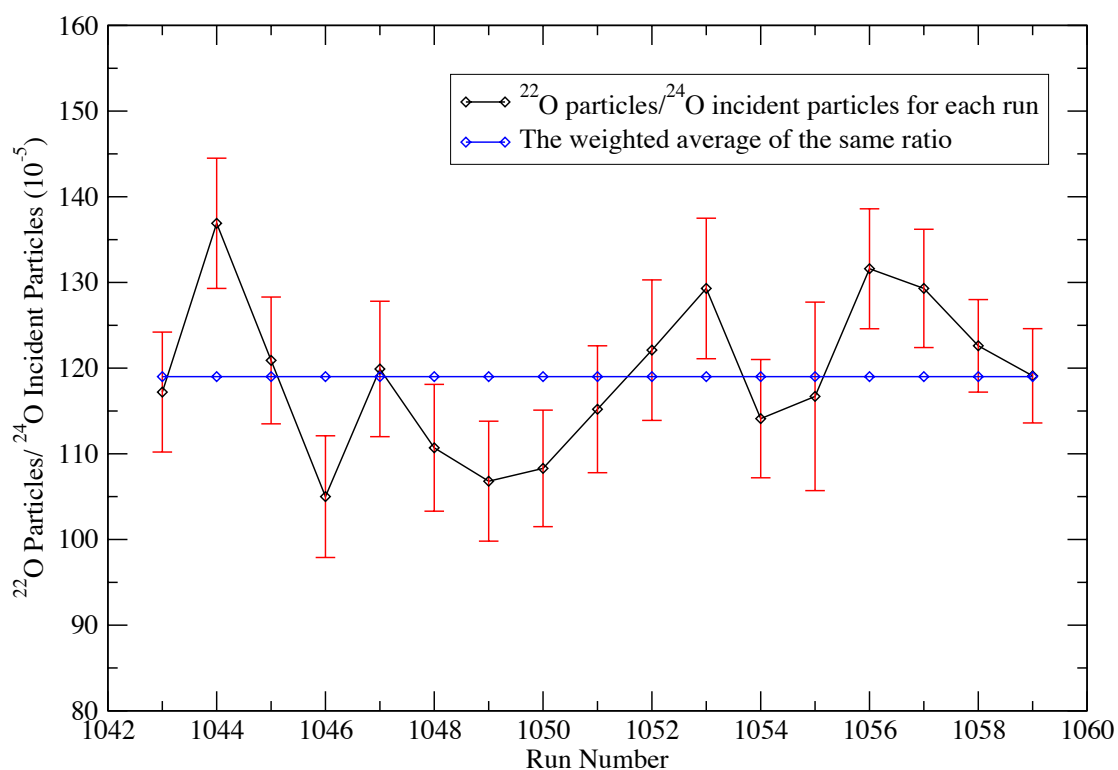
Figure 4.22: The ratio between the number of ^{22}O particles and incident ^{24}O particles with statistical uncertainties for all the production runs used in cross section calculation. The solid flat line represent the error weighted average of that ratio calculated for all those runs.

4.5.3 Systematic Uncertainties including Background Estimation

Although the calculated cross sections include background subtractions, the uncertainty in the background is mainly responsible for the systematic error in this experiment, and it gives rise to an important error in the final result. The background was taken as one half of the maximum plausible background under the peak. Figure 4.23 shows how this was done.
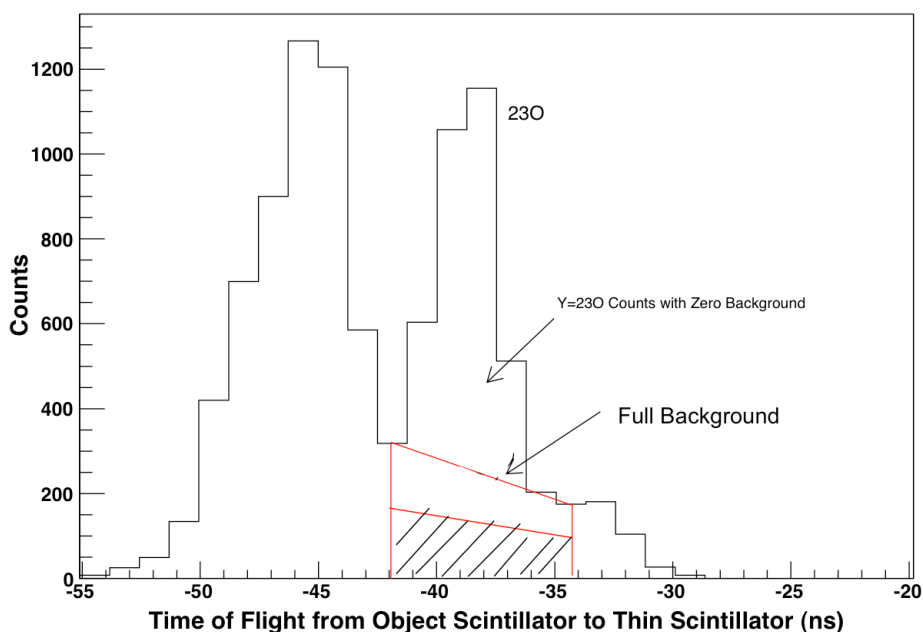
Figure 4.23: The combined production spectrum showing the background estimation for the ^{23}O setting.

From the first half of the experiment where the settings were focused on ^{23}O, the number of counts under the ^{23}O peak in the combined spectrum (combining all the

production runs in the first half) was 3730(61). The number of counts inside the full background shown in Figure 4.23 was 1593. So the background was estimated to be one half of that which is equal to 796.6(28.3). This estimation provides that about 78.6%(1.5%) of counts are from the actual signal while 21.4%(0.75%) are from the background.

For the second part of the experiment in the ^{22}O setting, the number of counts measured in a similar way to the above, lead to an uncertainty from the background which was only 1.04%. The Figure 4.24 shows the time of flight spectrum from the OBJ scintillator to the thin scintillator for the ^{22}O setting which was used for the isotope identification. However due to the possible particle contamination in the low energy regime under the ^{22}O peak we suggest a 5% uncertainty arises from the background for the two-neutron knockout cross section.
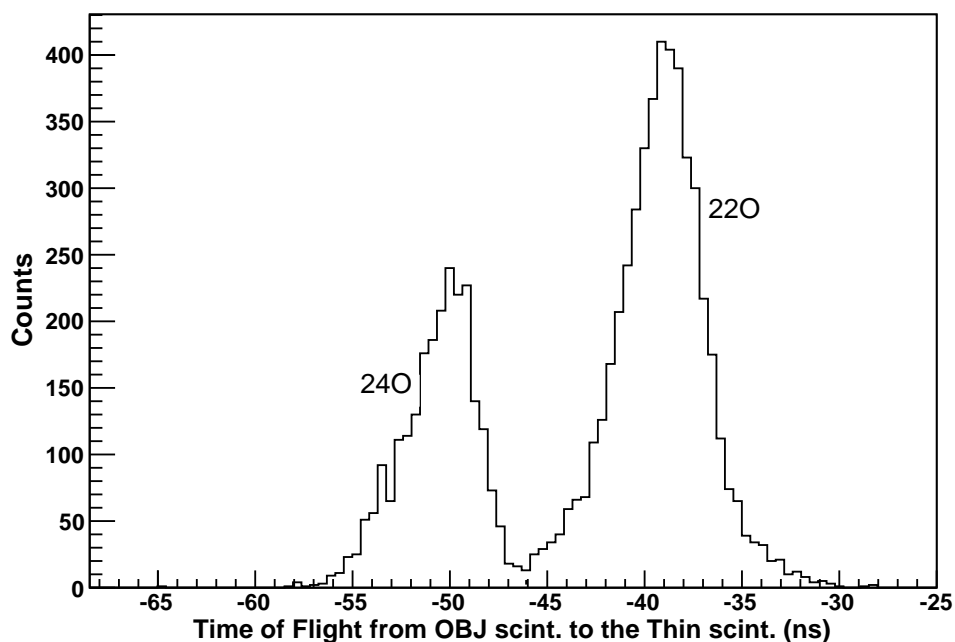
Figure 4.24: The combined production spectrum showing the background estimation for the ^{22}O setting.

Uncertainties coming from the changes in the beam purity and stability is about 5%, and the error accounting for the limited momentum acceptance of the S800 spectrograph is below 10%. The uncertainty of the reaction target thickness should also be considered for a full systematic error calculation. This was estimated to be 2% from the target manufacturer. The systematic uncertainties will add in quadratures to the statistical uncertainty and be presented in the final cross section value.

A complete set of systematic and statistical uncertainties are tabulated for the both settings in the table 4.5.

Table 4.5: Fractional systematic and statistical uncertainties for the cross sections.

Type of uncertainty	Amount	
	^{23}O setting	^{22}O setting
Background	0.21	0.05
Limited momentum acceptance of S800	0.10	
Beam purity and stability	0.05	
Uncertainty in the target thickness	0.02	
Statistical uncertainty	0.023	0.015
Total uncertainty	0.24	0.13

The neutron knockout cross section of ^{24}O to the ground state of ^{23}O was calculated using the total number of ^{23}O particles, the background estimation, the number of incident particles, target thickness, and efficiencies using the equation,

$$\sigma = \frac{(^{23}O - Background)}{(Incident\ Particles)\ t\epsilon}, \qquad (4.20)$$

which is,

$$\sigma = \frac{3730 - 796.5}{5424886.27 \times 0.0000126} mb. \qquad (4.21)$$

Here ϵ is 100% for the XFP, OBJ scintillator and CRDCs.

This cross section was calculated to be 42.9 mb with a statistical uncertainty of 1.0 mb. The statistical uncertainly is coupled with a total systematic uncertainly of 10 mb.

The two-neutron knockout cross section of ^{24}O when calculated using a same method was calculated to be 90.2 mb with a total uncertainty of 12 mb.

4.6 Longitudinal Momentum Distribution

In addition to the cross section measurements it is useful to obtain the momentum distribution in order to assign the angular momentum of the populated states. The energy, position, and angles after the S800 spectrograph were measured using the S800 charged particle detectors. However, for the angular momentum calculations we are interested in determining the positions, angles, and energy deviations before the magnet at the target position to get the momentum distribution of the residual nucleus. Determining these quantities at the target from the measured ones in the detectors is done using the inverse map which was obtained from the code COSY INFINITY from the National Superconducting Cyclotron Laboratory.

4.6.1 Inverse Map Calculations

The inverse map was used to reconstruct charged fragment four momentum vectors by determining the trajectories through the S800. In this way it is capable of measuring the x position and angle, position in the dispersive direction y, its angle at the target position, and the relative energy deviation $\delta = (E - E_0)/E_0$ where E is the kinetic energy of the beam and E_0 is the reference energy of the particle following the central trajectory [NF07].

The forward ion optical matrix can be defined as a matrix which relate the the coordinates $(x, \theta_x, y, \theta_y, \delta)^T$ at the target in front of the magnet and $(x, \theta_x, y, \theta_y, \Delta L)^D$ in the detector following the magnet. The quantity ΔL is the difference in the track length compared to the length of the central trajectory [NF07]. By measuring the quantities in the detector and, if we know the matrix elements of the optical matrix, then we can find the quantities at the target:

$$
\begin{pmatrix}
x \\
\theta_x \\
y \\
\theta_y \\
\Delta L
\end{pmatrix}^{(D)}
=
\begin{pmatrix}
M_{xx} & M_{x\theta_x} & 0 & 0 & M_{x\delta} \\
M_{\theta_x x} & M_{\theta_x \theta_x} & 0 & 0 & M_{\theta_x \delta} \\
0 & 0 & M_{yy} & M_{y\theta_y} & 0 \\
0 & 0 & M_{\theta_y y} & M_{\theta_y \theta_y} & 0 \\
M_{Lx} & M_{L\theta_x} & 0 & 0 & M_{L\delta}
\end{pmatrix}
\begin{pmatrix}
x \\
\theta_x \\
y \\
\theta_y \\
\delta
\end{pmatrix}^{(T)} .
\tag{4.22}
$$

In the central trajectory, x, y, θ_x and θ_y are all zero and the kinetic energy becomes E_0 because it is parallel to the beam line. In order to construct the matrix, we need to input the mass, and charge of the particle of interest, and currents in the 4 magnets of the S800 spectrograph in order to set it to account for certain magnetic rigidity. When we feed those values into the computer program COSY INFINITY, it will generate an ion-optical matrix. In the matrix, there are two non-zero 2×2 sub matrices M' which mix the positions and angles in dispersive and non dispersive directions [NF07]. Here, det M' =1 so there are only three independent parameters in each sub matrix. The central energy E_0 can be calculated through the equation [Mei12],

$$
E_0 = MA \left[\sqrt{1 + \left(\frac{Q}{M} \frac{B_{\rho 0}}{3.107} \right)^2} - 1 \right]
\tag{4.23}
$$

where M and Q represent the atomic mass and charge (note that the electrons in the Oxygen isotopes here are fully stripped) of the particle of interest along the central trajectory. The

quantity A is the atomic mass unit which is equal to 931.5 MeV, and $B_{\rho 0}$ is the measured magnetic rigidity which was 3.9 Tm in this case with an unit conversion factor of 3.107 [Mei12].

Positions and angles of particles measured at the detector are used to determine the energy, angles and positiosn at the reaction target. For this reason, the forward ion optical matrix introduces here should be inverted. In this inversion, it is not useful to have the full 5×5 matrix inversion because only first four quantities of the detector position are known (the track length is not a measured quantity). In both focusing and dispersion matched modes, either the x position of the target position $x^{(T)}$ is zero or negligibly small. So we can reconstruct the matrix in a way that the $\triangle L^{(D)}$ and $x^{(T)}$ are not included. This 4×4 matrix is now called the fully inverse ion optical matrix [NF07]:

$$
\begin{pmatrix} x \\ \theta_x \\ y \\ \theta_y \end{pmatrix}^{(D)} = \begin{pmatrix} M_{x\theta_x} & 0 & 0 & M_{x\delta} \\ M_{\theta_x\theta_x} & 0 & 0 & M_{\theta_x\delta} \\ 0 & M_{yy} & M_{y\theta_y} & 0 \\ 0 & M_{\theta_y y} & M_{\theta_y\theta_y} & 0 \end{pmatrix} \begin{pmatrix} \theta_x \\ y \\ \theta_y \\ \delta \end{pmatrix}^{(T)} . \tag{4.24}
$$

Using a program written to exchange coordinates in the ion optical matrix, forward ion-optical matrices were transformed into inverse ion-optical matrices. Since $x^{(T)}$, the x position at the target, is available as an input, $x^{(D)}$ and $\theta_x^{(D)}$ which are measured at the detector position are interchanged with $\theta_x^{(T)}$ and δ^T. Also $y^{(D)}$ and $\theta_y^{(D)}$ are exchanged with $y^{(T)}$ and $\theta_y^{(T)}$ [NF07]. After the exchange is completed, the partial inverse ion-optical matrix looks like,

$$
\begin{pmatrix} \theta_x^{(T)} \\ y^{(T)} \\ \theta_y^{(T)} \\ \delta^{(T)} \\ \Delta L^{(D)} \end{pmatrix}_{\text{output}} = M \begin{pmatrix} x^{(D)} \\ \theta_x^{(D)} \\ y^{(D)} \\ \theta_y^{(D)} \\ x^{(T)} \end{pmatrix}_{\text{input}} \tag{4.25}
$$

This process of reducing the matrix size produces the same result as the fully inverted optical matrix provided by the code COSY INFINITY. So the coefficients produced by the COSY to get the matrix elements can be directly utilized to calculate the positions, angles and the fractional energy of the particles at the target position when the measured positions and angles at the detector are known. The fractional energy δ^T which is given by,

$$
\delta^T = \frac{(E - E_0)}{E_0} \tag{4.26}
$$

is used to calculate the total momentum of the scattered particle. The dispersive and non-dispersive angles and the y position at the target were used to calculate the scattering angle of an event at the target position which is then used to obtain the parallel and perpendicular components of the total momentum. The method used for the momentum calculation using the position, angle information along with the kinetic energy of the beam was initially formulated by Dr. Krista C. Meierbachtol for her PhD thesis in 2012 [Mei12]. This was used as the key reference for the momentum distribution calculation of this experiment.

The total linear momentum is given by the equation,

$$
P = E \sqrt{1 + \frac{2MA}{E}} \tag{4.27}
$$

where *M* stands for the mass of the isotope of interest in MeV and *A* is the atomic mass unit which is equal to 931.5 in MeV. The quantity *E* is the kinetic energy of the particle which is calculated using the equation 4.26 [Mei12].

4.6.2 Momentum Calculations

Parallel and perpendicular momenta are constructed using the positions, angles and fractional energy of each isotope at the target position as described earlier. This information at the target is extracted from the inverse matrix coefficients that were obtained for each different oxygen isotope by inputing the specific information such as the set B-rho value and magnetic current settings used during the experiment. The coefficients were calculated by using the COSY INFINITY code written by the NSCL which is a combination of fortran codes and codes from high level COSYScript language. They were used to deduce the four quantities for every event, dispersive and non-dispersive angles, non-dispersive position and the fractional energy at the target using the measured positions and angles at the detector. Those measurements for ^{23}O are shown in Figures 4.25, and 4.26.
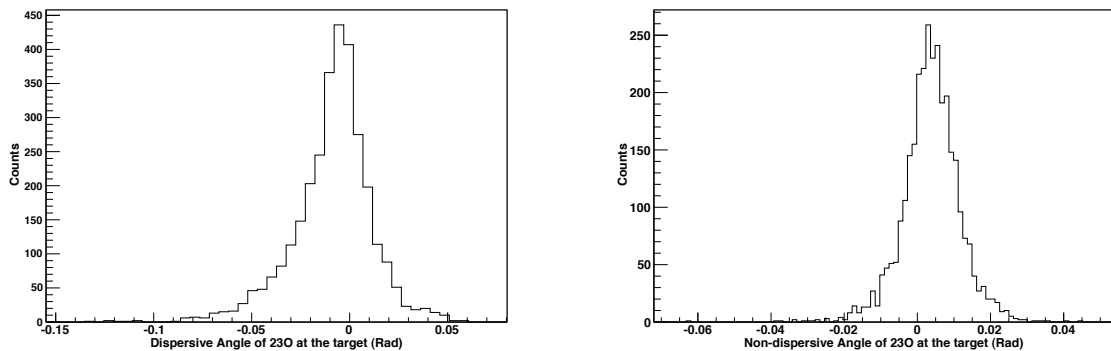
Figure 4.25: Dispersive (left) and Non-dispersive (right) angles of ^{23}O at the target.
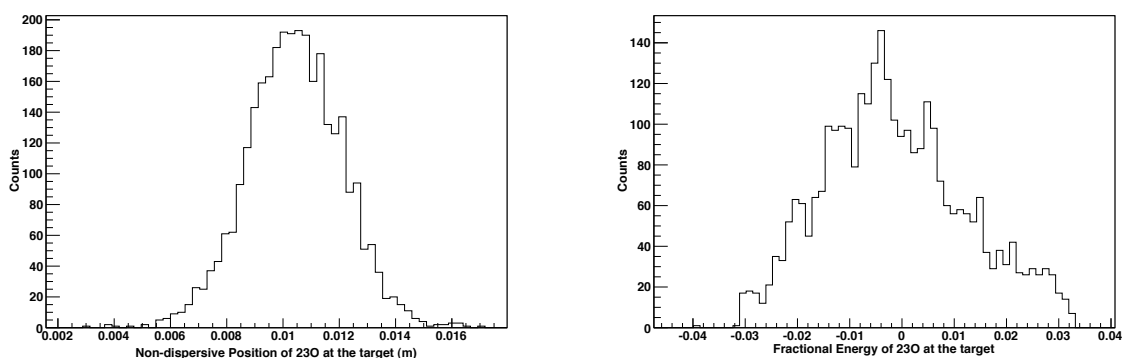
Figure 4.26: Non-dispersive position (left) and fractional energy (right) of ^{23}O at the target.

The quantities E_0 and E were calculated using the equations 4.23 and 4.26, respectively, after δ^T was extracted from data. E_0 and E for ^{23}O are shown in Figure 4.27. The total linear momentum, P of ^{23}O at the target was deduced from the energy using mass relationship shown in the equation 4.27 and is shown in the Figure 4.28.
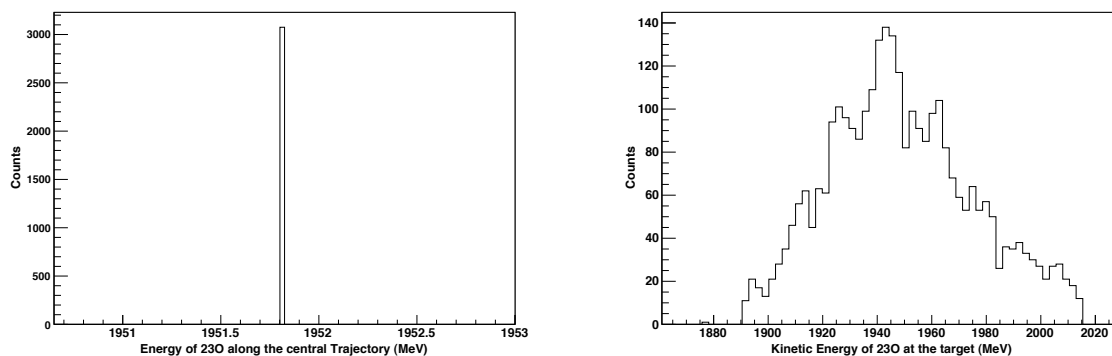
Figure 4.27: The energy of ^{23}O along the central trajectory (left) and total kinetic energy of ^{23}O at the target (right).
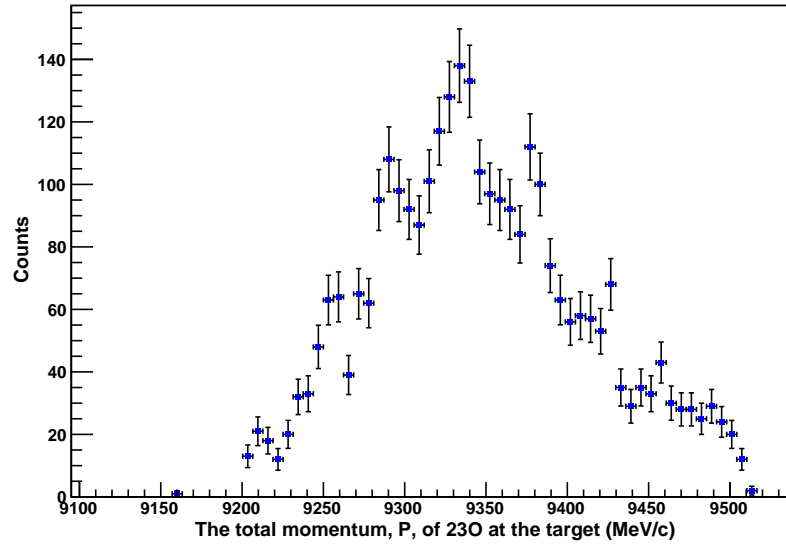
Figure 4.28: The total momentum, P, of ^{23}O at the target in the lab frame.

The scattering angle for an event is defined using the dispersive and non-dispersive angles at the target position as shown in the equation,

$$\theta = \arcsin \sqrt{\sin^2 \theta_x^T + \sin^2 \theta_y^T} \tag{4.28}$$

and is shown in Figure 4.29.
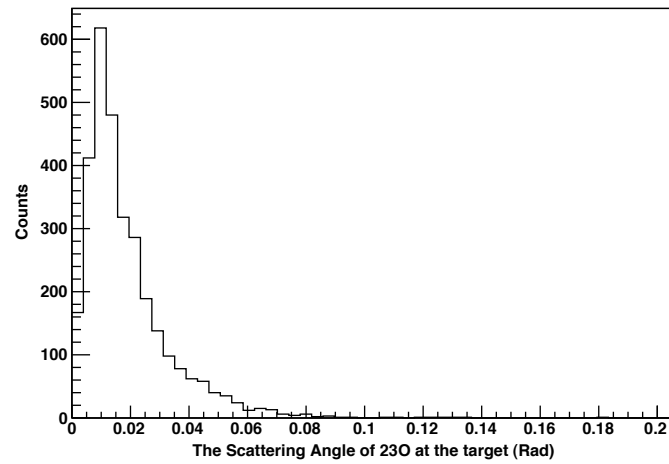
Figure 4.29: The scattering angle of ^{23}O at the target.

The parallel and perpendicular components of the linear momentum were then deduced from P, the total linear momentum and the trigonometric relationships of the scattering angle as shown in the following equations,

$$P_{\parallel} = P\cos\theta, \tag{4.29}$$

and

$$P_{\perp} = P\sin\theta \tag{4.30}$$

and are shown in Figures 4.30 and 4.31 respectively.
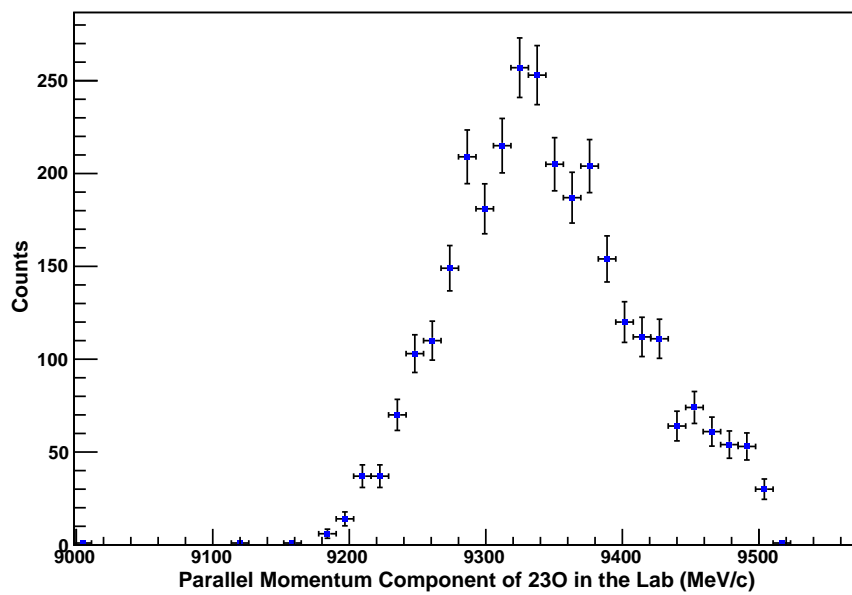
Figure 4.30: The parallel component of the ^{23}O total momentum in the lab frame.

Figure 4.31: The perpendicular component of the ^{23}O total momentum in the lab frame.

The parallel component of the linear momentum is much larger than the perpendicular components and thus the parallel component was taken as the total momentum of ^{23}O. This is understandable because the perpendicular component is usually very small compared to parallel component when doing a one-nucleon knockout reaction. All three momentum distributions shown above are in the lab frame and need to be converted into the center of mass system in order to be compared with a theoretical calculation of the momentum if any. The longitudinal momentum distribution in the projectile rest frame was obtained by performing the Lorentz transformation given by the relation,

$$P_{\|CM} = \gamma(P_{\|} - \beta E_{tot}), \tag{4.31}$$

where

$$E_{tot} = (\delta^T E_{0tot}) + E_{0tot} \tag{4.32}$$

and δ^T is the fractional energy which is described in chapter 2. Here,

$$E_{0tot} = MA\left[\sqrt{1 + (\frac{Q}{M}\frac{B_{\rho 0}}{3.107})^2} \right]. \tag{4.33}$$

The quantities γ and β for ^{23}O isotope were calculated inputting the LISE++ velocity of the particles at the target using the general definition of Lorentz factor:

$$\gamma = \frac{1}{\sqrt{1 - \frac{v^2}{c^2}}} = \frac{1}{\sqrt{1 - \beta^2}}. \tag{4.34}$$

The Lorentz factor γ and β of ^{23}O were calculated to be 1.0912 and 0.4367 respectively. Figure 4.32 shows the parallel momentum distribution of ^{23}O in the center of mass system after converting using the above shown Lorentz transformation.
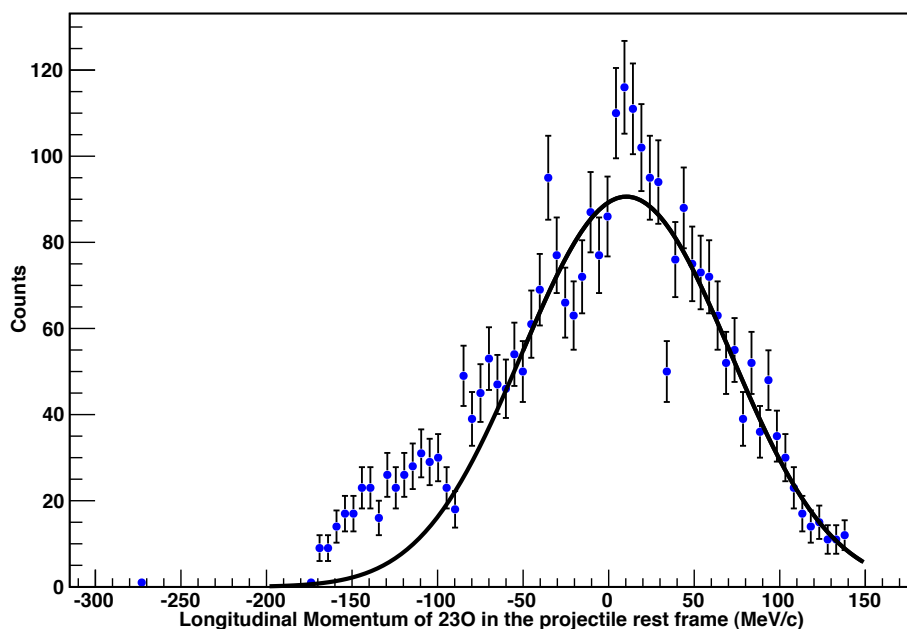
Figure 4.32: The parallel component of the linear momentum of ^{23}O in the center of mass system.

The experimental momentum distributions should be well described by gaussians and momentum widths and peak positions have been discussed in the literature [Mei12]. It has been discovered that the widths of the momentum distributions depends on the masses of the projectile and fragment but not on the target type or its mass [Mei12]. Although the shape of the momentum distribution should be well-fitted with a gaussian it's not always the case when it comes to reactions that take place after the the projectile goes through the A1900 fragment separator. Due to the large momentum bite taken from the A1900 (1% momentum acceptance in this case) the shape of the momenta will not be well fitted by a Gaussian. The width of the ^{23}O is defined to be the full width at half maximum of its momentum distribution. However, to get the proper width, we have to remove the resolution of the S800 spectrometer from this number. The resolution of S800 was

measured by plotting the parallel momentum of unreacted ^{24}O through the target using the unreacted runs with the ^{24}O centered in the focal plane with the target.

The parallel momentum of ^{24}O was extracted using the same methodology used in computing the ^{23}O parallel momentum. Once the parallel momentum of ^{24}O is obtained, it was converted to the projectile rest mass by using the Lorentz transformation with calculated γ and β for ^{24}O which were 1.099 and 0.456 respectively. The Parallel momentum of ^{24}O in the lab frame and in the projectile rest frame are shown in Figures 4.33 and 4.34 respectively.

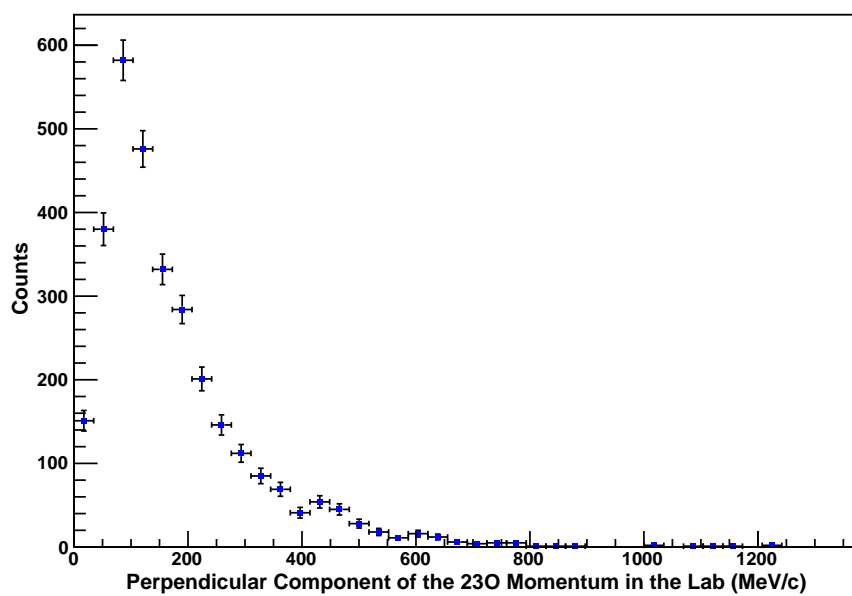Figure 4.33: The parallel component of the total momentum of ^{24}O in the lab frame. The solid curve is a fit done with a convolution of a gaussian function with a square function.
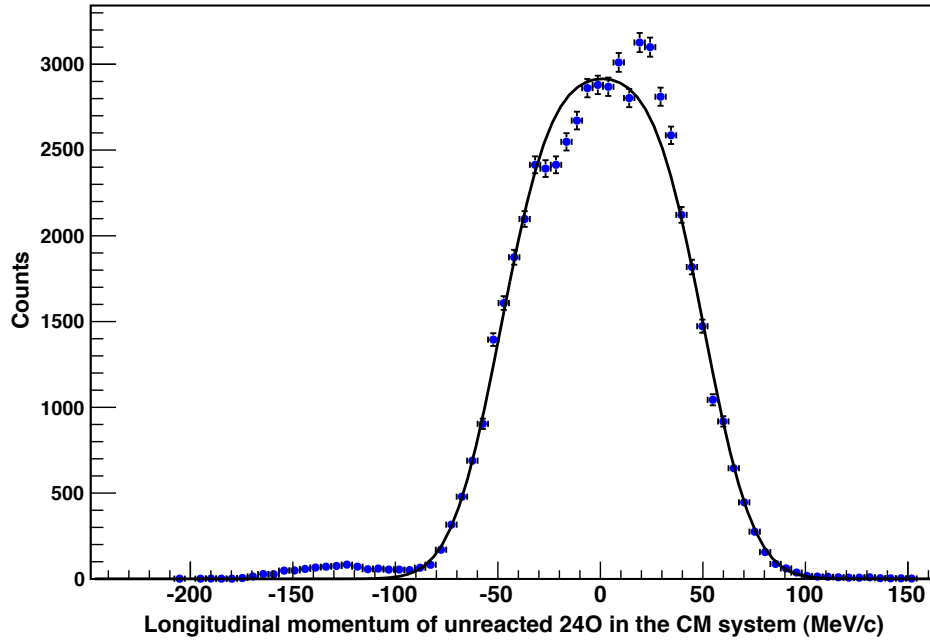
Figure 4.34: The longitudinal momentum of ^{24}O in the projectile rest frame. The solid curve is a fit done with a convolution of a gaussian function with a square function.

Similar to the ^{23}O momentum distribution, the ^{24}O momentum as well will not be well fitted with a gaussian due to the large momentum bite taken from the A1900 fragment separator. The flat peak present in the distribution with gaussian tails will be better fitted with a convolution of a gaussian function with a square function. To obtain the momentum width of ^{23}O, this function should be convoluted with another gaussian in order to reproduce the measured ^{23}O distribution. However, if this function is convoluted with another gaussian, it gives back the same functional form but with

$$\sigma = \sqrt{\sigma_1^2 + \sigma_2^2}. \tag{4.35}$$

In order to obtain the ^{23}O momentum width, both ^{23}O longitudinal momentum and unreacted ^{24}O longitudinal momentum in the projectile rest frame were fitted with the function which is the convolution of a gaussian and a rectangle.

The width (FWHM) of the ^{24}O momentum which represents the resolution of the S800 spectrograph was found to be 98.8 MeV/c with an uncertainty of 19.2 MeV/c when fitted with a convolution function. The momentum distribution for one-neutron removal from ^{24}O is fitted with the same function and has determined the value of σ. When fitting the momentum range was selected to be from -51 MeV/c to 150 MeV/c. This was done to eliminate the data (extra bump at the low momentum side) coming from the multiple scattering events at the target or any elastic/inelastic scattering occurred which are not from the reaction of interest. The two σ values deduced by the fits were then subtracted in quadrature to get the width of the gaussian function and multiplied by the number 2.3548 to which represents the measured ^{23}O momentum distribution. The resulting ^{23}O longitudinal momentum distribution in the projectile rest frame has a width of 112(8) MeV/c (with statistical error only).

The parallel momentum of ^{22}O was extracted using the same methodology used in computing the ^{23}O parallel momentum and it was converted to the projectile rest mass by using the Lorentz transformation with calculated γ and β for ^{22}O which were 1.100 and 0.417 respectively. The Parallel momentum of ^{22}O in the lab frame a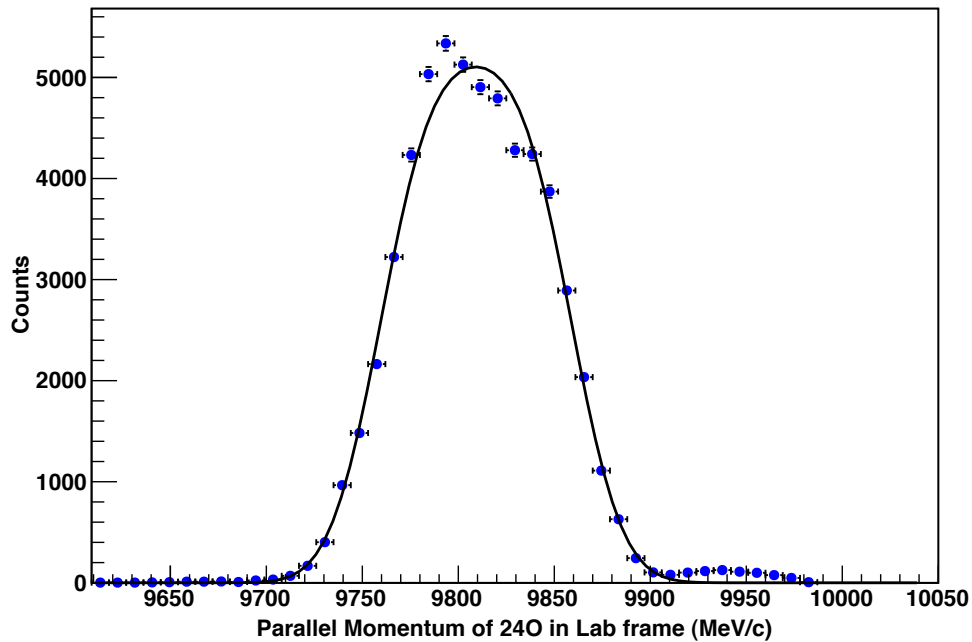nd in the projectile rest frame is shown in Figure 4.35. When folding in with the resolution of the S800 spectrograph (found using the ^{24}O parallel momentum distribution) the width of the ^{22}O momentum was measured to be 241(42) MeV/c.
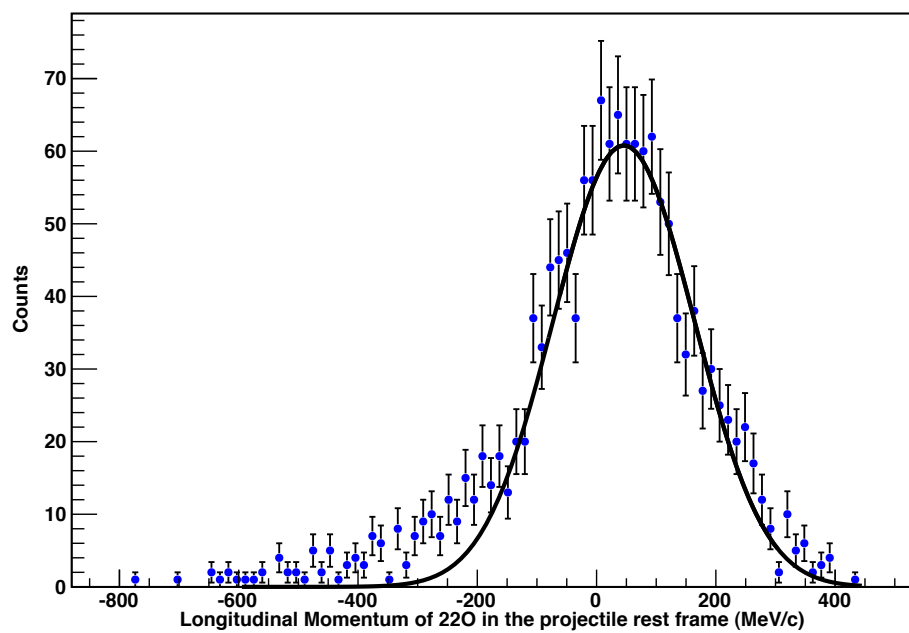
Figure 4.35: The longitudinal momentum of ^{22}O in the projectile rest frame.

5   DISCUSSION

5.1   Model Calculations

All the model calculations of the neutron removal reaction of ^{24}O were done by Dr. Jeff Tostevin from University of Surrey, UK. The following explanation of the calculational methods is based on his recent article [Tos01].

The calculations of single particle cross-sections σ_{sp} require the eikonal elastic scattering S matrices between neutron and target as well as residue and target. These matrices are calculated with the help of static density limit of the Glauber multiple scattering series as shown in the Ref. [AKTT96]. The S matrices are calculated using the absorptive neutron-^{9}Be target interaction and ^{23}O residual-^{9}Be target interaction. The single-folding $t_{NN}\rho_t$ model was used for the nucleon and double-folding $t_{NN}\rho_r\rho_t$ model for the residue ^{23}O. The density of ^{23}O was calculated by spherical Hartree-Fock (HF) using the SkX Skyrme interaction [AB98]. The ^{9}Be target density takes a Gaussian form with a point-nucleon root-mean squared radius of 2.36 fm.

The bound neutron single-particle wave functions in ^{24}O were constructed as eigenstates of Woods-Saxon potentials with radius r_0 and and diffuseness parameter a_0 are being equal to 0.7 fm. A spin-orbit potential having the same radius and diffuseness parameters was also included with a fixed strength of V_{so}=6.0 MeV. Spherical Hartree-Fock calculations for ^{24}O control the values of the r_0 for the neutron sd-shell orbitals [GAB$^+$08]. This is due to the required consistency between the radial extent of the wave functions and the extent of the calculated ^{23}O density that is used for the determination of its absorptive optical model potential. For the $2s_{1/2}$ orbital, r_0=1.0184 fm while for the $1d_{5/2}$ orbital, r_0=1.1735 fm. Depths of the binding potential for these single-particle orbitals are tuned to mimic the fitting S_n^* value for each final state.

5.2 Results

Table 5.1 shows the theoretical prediction of the partial and inclusive cross section values for the ^{9}Be(^{24}O,^{23}O(ground state)), ^{9}Be(^{24}O,^{23}O(5/2$^+$ first excited state)) reactions and direct 2n removal reaction at 92.3 MeV. Also included are the measured cross sections in this study, 42.9 mb with an uncertainly of 29% and 90.2 mb with 13% uncertainty for above reactions, respectively. The measured energy was used for the excited (5/2$^+$) final state. For details of the measurements readers are referred to the Ref. [SFB$^+$07]. The spectroscopic factors from the SDPF-M effective interaction listed in the table were obtained from the first table of Ref. [KNP$^+$09].

Table 5.1: The theoretical prediction of the partial for the ^{9}Be(^{24}O,^{23}O(ground state)), ^{9}Be(^{24}O,^{23}O(5/2$^+$ first excited state)) reactions and direct 2n removal reaction at 92.3 MeV. The inclusive cross section which is the summation of all three above mentioned cross sections is also included. The total ^{22}O yield is the summation of ^{9}Be(^{24}O,^{23}O(5/2$^+$ first excited state)) reaction cross section and direct 2n removal reaction cross section. Both these reactions have same ^{22}O end product as the first excited state of ^{23}O immediately decays into ^{22}O by emitting a neutron. Also included in the table are the spectroscopic factors obtained from SDPF-M shell model and measured cross section values.

E^* (MeV)	J^π	C^2S	C^2S	σ_{sp} (mb)	σ_{th} (mb)	σ_{exp} (mb)
0.00	1/2$^+$	1.769	–	36.20	69.7	42.9(10.3)
2.78	5/2$^+$	–	5.593	19.43	118.3	
-2n	direct				29.9	
	^{22}O yield				148.2	90.2(11.7)
	inclusive				217.9	133.1(22)

The spectroscopic factors given by the USD-B shell-model interaction [BR06] are in good agreement with the SDPF-M shell model calculations giving C^2S (1/2$^+$)=1.810 and C^2S (5/2$^+$)=5.665 [KNP$^+$09].

The longitudinal momentum distribution of the residual ^{23}O is calculated using the elastic S matrix inputs [BH04] using the same bound state. The longitudinal momentum distribution of ^{22}O is also calculated but in this case there is an additional recoil broadening of about 18 MeV/c which is negligibly small compared to the momentum width. This additional broadening is a result of the residue being unbound by 45(2) keV with respect to the first neutron threshold of 2.734 MeV [MWP12]. The theoretically predicted parallel momentum distributions for the ^{9}Be(^{24}O,^{23}O) reaction at 100 MeV/nucleon is shown in Figure 5.1. Previous simillar measurements give information on the widths of parallel momentum distribution of the knockout reaction and they agree with both measured and calculated values of the present work. Reference [KNP$^+$09] gives ^{9}Be(^{24}O,^{23}O (ground state))) parallel momentum to have a width of 99(4) MeV/c.
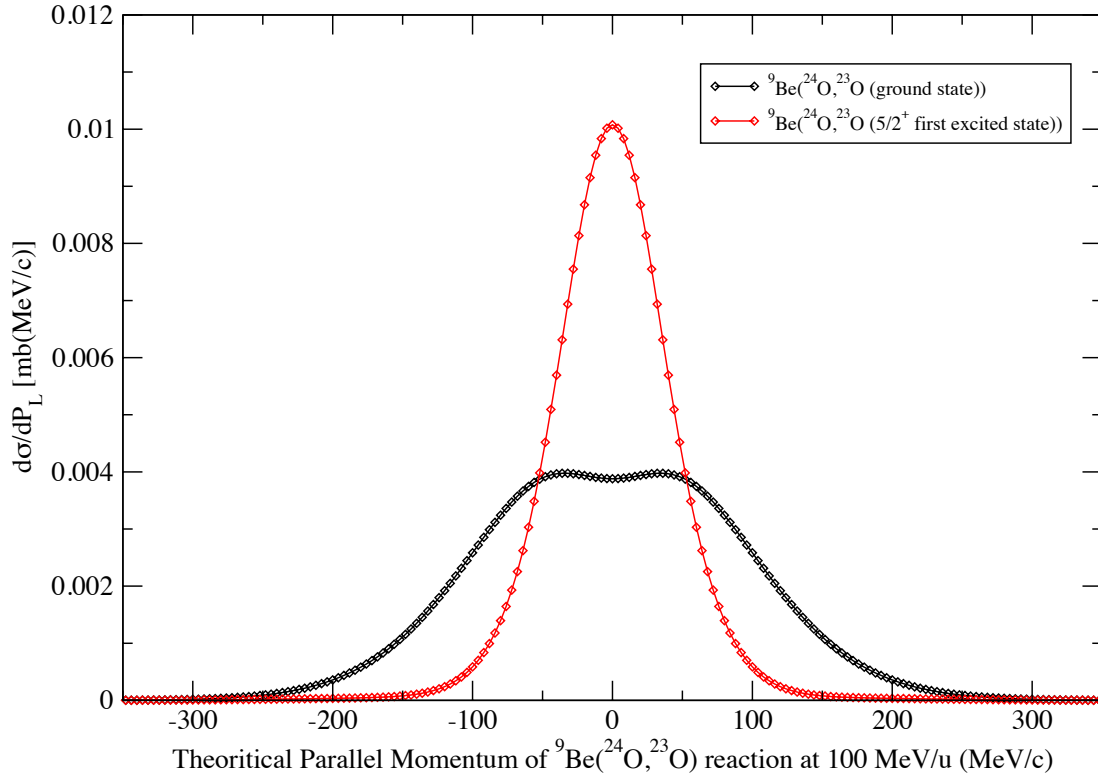
Figure 5.1: The theoretically predicted parallel momentum distributions for the ^{9}Be(^{24}O,^{23}O) reaction at 100 MeV/nucleon.

The inclusive $2n$ removal cross section of ^{24}O is calculated by considering all the smaller contributions that populate the several bound final states of the ^{22}O residue through the direct two neutron removal reactions. These smaller cross sections are calculated by the eikonal model generalized for $2n$ removal processes [TPBH04, TB06] using the shell-model two-nucleon amplitudes (TNAs), and the radius of the bound neutron r_0. The two neutron separation energy of ^{24}O is S$_{2n}$(g.s.)=6.926 MeV and average separation energy of each nucleon is equal to $\bar{S}_n^* = [S_{2n}(\text{g.s.})+E_{22}^*]/2$ for the given final state. The S-matrix is

computed using the spherical Hartree-Fock density of ^{22}O. Table 5.2 tabulate partial direct

2n removal cross sections to all theoretically (shell model) predicted bound states of ^{22}O.

The inclusive 2n removal cross-section of 22.9 mb is the combined value of all the small

cross sections shown in Table 5.2 and is added to the theoretical ^{22}O production yield in

Table 5.1.

Table 5.2: Theoretical direct two-neutron removal reaction cross sections, $\sigma_{th}(-2n)$, from ^{24}O to all predicted ^{22}O(J^π, E^*) shell-model final states below the first neutron threshold of 6.85 MeV [MWP12].These cross sections are calculated using USD-B interactions [BR06]. The calculations are for the ^{9}Be target and ^{24}O energy of 92.3 MeV/nucleon.

E^* (MeV)	J^π	σ_{th}(-2n)(mb)
0.000	0^+	3.71
3.158	2^+	8.48
4.762	0^+	1.09
4.795	3^+	5.33
6.363	2^+	4.16
6.734	4^+	7.12
$-2n$	inclusive	29.88

The ratio between the experimental cross section and theoretical cross section, $R_s=\sigma_{exp}/\sigma_{th}$ deduced for the ^{9}Be(^{24}O,^{23}O(ground state)) reaction is R_s=0.62(0.09) and is consistent with previously observed systematics [GAB$^+$08, Tos12] for one neutron removal reactions of neutron rich isotopes.

The single particle cross sections for unit spectroscopic factors are 36.20 mb and 19.43 mb for (1/2$^+$) and (5/2$^+$) states respectively when calculated using the above discussed theoretical models. Using the measured cross section values to get the ratio between

measured and theoretical cross sections, the data indicate spectroscopic factors of order 1.2 and 4.6 for ($1/2^+$) and ($5/2+$) states, respectively. The experimental spectroscopic factors are subjected to uncertainties arising from the uncertainties in the experimental cross section (24% for the one neutron removal and 13% for the two neutron removal) and theoretical cross section. However the errors in the theoretical cross sections are unknown and thus cannot be included in the uncertainty of the experimental spectroscopic factors. The measured experimental spectroscopic factors reasonably agree with the SDPF-M as well as USDB shell model calculations and confirm the spherical shell closure at N=16 in ^{24}O making it a Doubly Magic Nucleus.

6 CONCLUSION

6.1 Summary

Establishing the ground state wave-function of ^{24}O and its doubly magic nature through one and two neutron knockout cross section measurements of ^{24}O were the main focus and goals of this work. The experiment was conducted in the S3 vault of the National Superconducting Cyclotron Laboratory (NSCL) at Michigan State University using the S800 spectrograph. In the experiment, a secondary beam of ^{24}O was produced with a 1% momentum spread using a primary beam of ^{48}Ca at 140 MeV/u and a 1551-mg/cm^2-thick Be production target.

The secondary beam expected from the production target is ^{24}O, but it includes many impurities. In order to have a more pure beam, the A1900 fragment separator was used. The energy of the ^{24}O beam was 92.3 MeV/u. The components in the S800 beam line are used to monitor and to calibrate the secondary beam by using specific information such as time of flight details. The two cathode readout drift chambers (CRDCs) are used to measure the position and the angle of the charged particles. The second CRDC detector is followed by an ion chamber for energy loss measurements and one plastic scintillator and and a hodoscope to provide a reference time to measure the drift time of the electrons inside the CRDCs.

The neutron knockout cross sections of ^{24}O to the ground state of ^{23}O was found using the numbers of ^{23}O and incoming ^{24}O counted. The neutron knockout cross section from the ^{24}O ground state to ^{23}O ground state was determined to be 42.9 mb with an uncertainty of 24%. The two neutron knockout cross section from ^{24}O ground state was found to be 90.2 mb with a 13% uncertainty using the number of ^{22}O counts by considering ^{22}O counts as coming from the breakup of the first excited state of ^{23}O or coming directly from ^{24}O by two neutron removal reaction. The biggest contribution for

the error estimation was coming from the background and was 21%. Only 1.7% was from statistical uncertainties and there was a total additional systematic error of 11% resulting from the limited momentum acceptance of S800 spectrograph, and uncertainties in beam purity and in the target thickness.

The theoretical cross section calculated using the spectroscopic factors found by the SDPF-M shell model were performed by Dr. Jeff Tostevin from University of Surrey, UK. The predicted cross sections for the $9Be(^{24}O,^{23}O$(ground state)), $^{9}Be(^{24}O,^{23}O(5/2^{+}$ first excited state)) reactions and direct $2n$ removal reaction at 92.3 MeV were 69.7 mb, 118.3 mb, and 148.2 mb, respectively. The inclusive measured cross section was 133(16) mb for all possible neutron removal reactions of ^{24}O while the theoretical inclusive cross section gave the value of 217.9 mb. The single particle cross sections per unit spectroscopic factor, 36.20 mb and 19.43 mb, for the $9Be(^{24}O,^{23}O$(ground state)) and direct $2n$ removal reaction respectively, indicate spectroscopic factors of order 1.2 and 4.6 for (1/2+) and (5/2+) states respectively, and reasonably agree with the SDPF-M as well as USDB shell model calculations. The ratio between the measured cross section and the theoretically predicted cross section, $R_s=\sigma_{exp}/\sigma_{th}$, was calculated to be 0.62(0.09) and is consistent with similar previous measurements [GAB+08, Tos12].

The longitudinal momentum distributions of unreacted ^{24}O, ^{23}O, and ^{22}O in the projectile rest frame were also measured. The experimental resolution was modeled as the convolution of a rectangle and a gaussian, with the parameters determined from a fit to the unreacted ^{24}O. The widths of the momentum distributions (full width at half maximum of the gaussian) were found to be 112(8) MeV/c for ^{23}O and 241(42) MeV/c for ^{22}O.

6.2 Outlook

The data presented in this work provide one and two neutron knockout cross sections of ^{24}O to the ground state of ^{23}O and to the neutron unbound ^{22}O and also give the

linear momentum distribution of fragmentation products in the transition region where the fragmentation mechanism occurs. The cross section measurements to the ground state of ^{23}O is a new result which provides important parameters for the determination of ^{24}O ground state wave function and indicate how doubly magic ^{24}O really is. However, the complete ground state wave function is yet to be established. For example, the one neutron knockout cross section of ^{24}O to the first excited state of ^{23}O remains to be measured. This followup experiment was conducted as the second part of the present experiment that is discussed in here. It measured this cross section by measuring the unbound neutron emitted when ^{23}O immediately decays into ^{22}O. This experiment is being analyzed by the same MoNA collaboration and results are still pending. Once available, these cross section values to the different final states of ^{23}O along with the related spectroscopic factors will convey us a very complete composition of the ^{24}O ground state wave function.

The establishment of the ground state wave function of ^{24}O will be advantageous for understanding the nuclear structure of isotopes near the drip line which have unusual proton to neutron ratios. The results of this research will build a foundation for a variety of other experiments to explore more about the isotopes that have only been investigated by theory.

Nuclei near the drip line away from nuclear stability are not common on earth due to the fact that there are no naturally occurring nuclei on Earth which undergo proton emission or neutron emission towards the line of stability. Most such neutron or proton rich isotopes are naturally found in stars with extreme temperature and pressure conditions. Studying the nuclei near the neutron drip line is important in nuclear astrophysics as they provide limitations and boundaries for explosive nucleosynthesis in environments such as neutron stars having with these extreme pressures, and temperatures. Further studies of nuclei in this regime will help understand the nucleosynthesis process more deeply.

The series of experiments conducted to investigate ^{24}O will provide much important feedback for the ongoing discussion regarding how to propose new experiments for other

neutron rich isotopes. Neutron-rich doubly magic nuclei and other nuclei near the neutron drip line continue to intrigue nuclear physicists.

REFERENCES

[AB98] B. Alex Brown. New skyrme interaction for normal and exotic nuclei. *Phys. Rev. C*, 58:220–231, Jul 1998.

[AKTT96] J. S. Al-Khalili, J. A. Tostevin, and I. J. Thompson. Radii of halo nuclei from cross section measurements. *Phys. Rev. C*, 54:1843–1852, Oct 1996.

[Ban09] Benjamin Banier. Woods saxon potential for a=50, at units of fermi, relative to v0, a=0.5fm. 2009. http://skipper.physics.sunysb.edu/~benjamin/ws/[Online; accessed Mar-2014].

[BBC⁺03] D. Bazin, A. Brown, B. M. Campbell, C. A. Church, J. C. Dinca, D. J. Enders, A. Gade, T. Glasmacher, G. Hansen, P. W. F. Mueller, H. Olliver, C. Perry, B. M. Sherrill, B. J. R. Terry, and A. Tostevin, J. ˙ New direct reaction: Two-proton knockout from neutron-rich nuclei. *Phys. Rev. Lett.*, 91:012501, Jun 2003.

[BH04] C. A. Bertulani and P. G. Hansen. Momentum distributions in stripping reactions of radioactive projectiles at intermediate energies. *Phys. Rev. C*, 70:034609, Sep 2004.

[BR06] B. Alex Brown and W. A. Richter. New usd hamiltonians for the sd shell. *Phys. Rev. C*, 74:034315, Sep 2006.

[bri] http://kids.britannica.com/elementary/art-647/ First-ionization-energies-of-the-elements[Online; accessed Mar-2014].

[Bro] B. A. Brown. Lecture notes in nuclear structure physics. Michigan State University, 2011.

[Bro01] B. Alex Brown. The nuclear shell model towards the drip lines. *Progress in Particle and Nuclear Physics*, 517:47, 2001.

[crd] http://www.nscl.msu.edu/files/s800_sld.pdf[Online; accessed Mar-2014].

[DB03] B. M. Sherrill J. Yurkon A. Zeller D. Bazin, J. A. Caggiano. The s800 spectrograph. *Nuclear Instruments and Methods in Physics Research Section B: Beam Interactions with Materials and Atoms*, 204:629–633, 2003.

[EDA⁺07] Z. Elekes, Zs. Dombrádi, N. Aoi, S. Bishop, Zs. Fülöp, J. Gibelin, T. Gomi, Y. Hashimoto, N. Imai, N. Iwasa, H. Iwasaki, G. Kalinka, Y. Kondo, A. A. Korsheninnikov, K. Kurita, M. Kurokawa, N. Matsui, T. Motobayashi, T. Nakamura, T. Nakao, E. Yu. Nikolskii, T. K. Ohnishi, T. Okumura, S. Ota, A. Perera, A. Saito, H. Sakurai, Y. Satou, D. Sohler, T. Sumikama, D. Suzuki, M. Suzuki, H. Takeda, S. Takeuchi, Y. Togano, and Y. Yanagisawa.

Spectroscopic study of neutron shell closures via nucleon transfer in the near-dripline nucleus o23. *Phys. Rev. Lett.*, 98:102502, Mar 2007.

[End90]   P. M. Endt. *Nuclear Physics A521*, 1, 1990.

[Fra06]   Nathan Henry Frank. *Spectroscopy of Neutron Unbound States in Neutron Rich Oxygen Isotopes*. PhD thesis, Michigan State University, 2006.

[GAB⁺08] A. Gade, P. Adrich, D. Bazin, M. D. Bowen, B. A. Brown, C. M. Campbell, J. M. Cook, T. Glasmacher, P. G. Hansen, K. Hosier, S. McDaniel, D. McGlinchery, A. Obertelli, K. Siwek, L. A. Riley, J. A. Tostevin, and D. Weisshaar. Reduction of spectroscopic strength: Weakly-bound and strongly-bound single-particle states studied using one-nucleon knockout reactions. *Phys. Rev. C*, 77:044306, Apr 2008.

[Hof09]   Calem R. Hoffman. *Investigation of the Neutron-Rich Oxygen Isotopes at the Drip Line*. PhD thesis, Florida State University, 2009.

[IGB⁺98] R. W. Ibbotson, T. Glasmacher, B. A. Brown, L. Chen, M. J. Chromik, P. D. Cottle, M. Fauerbach, K. W. Kemper, D. J. Morrissey, H. Scheit, and M. Thoennessen. Quadrupole collectivity in 32, 34, 36, 38si and the n=20 shell closure. *Phys. Rev. Lett.*, 80:2081–2084, Mar 1998.

[Kle01]   Heiko Klein. Shell-model for dummies. Technical report, 2001. http://www.ikp.uni-koeln.de/misc/doc/smfd/.

[KNP⁺09] R. Kanungo, C. Nociforo, A. Prochazka, T. Aumann, D. Boutin, D. Cortina-Gil, B. Davids, M. Diakaki, F. Farinon, H. Geissel, R. Gernhäuser, J. Gerl, R. Janik, B. Jonson, B. Kindler, R. Knöbel, R. Krücken, M. Lantz, H. Lenske, Y. Litvinov, B. Lommel, K. Mahata, P. Maierbeck, A. Musumarra, T. Nilsson, T. Otsuka, C. Perro, C. Scheidenberger, B. Sitar, P. Strmen, B. Sun, I. Szarka, I. Tanihata, Y. Utsuno, H. Weick, and M. Winkler. One-neutron removal measurement reveals o24 as a new doubly magic nucleus. *Phys. Rev. Lett.*, 102:152501, Apr 2009.

[KT10]   T. Nakamura N. Aoi H. C. Bhang S. Choi S. Deguchi F. Delaunay J. Gibelin T. Honda M. Ishihara Y. Kawada Y. Kondo T. Kobayashi N. Kobayashi F. M. Marques M. Matsushita Y. Miyashita T. Motobayashi Y. Nakayama N. A. Orr H. Otsu H. Sakurai S. Shimoura D. Sohler T. Sumikama S. Takeuchi K. N. Tanaka N.Tanaka Y. Togano K. Yoneda K. Yoshinaga T. Zheng Z. H. Li Z. X. Cao K. Tshoo, Y. Satou. Measurement of unbound excited states of 24o. *Journal of the Korean Physical Society*, 59:15291532, 2010.

[mag]   http://www.meta-synthesis.com/webbook/34_qn/qn_to_pt.html[Online; accessed Mar-2014].

[May48]   M. G. Mayer.   On closed shells in nuclei.   *Phys. Rev. Lett.*, 74:235–239, Mar 1948.

[Mei12]   Krista C. Meierbachtol. *Parallel and Perpendicular Momentum Distributions in Projectile Fragmentation Reactions*. PhD thesis, Michigan State University, 2012.

[MWP12]   A.H. Wapstra F.G. Kondev M. MacCormick X. Xu M. Wang, G. Audi and B. Pfeiffer.   The ame2012 atomic mass evaluation.   *Chinese Physics C*, 36, 2012.

[NF07]   D. Bazin W.A. Peters M. Thoennessen N.H. Frank, A.Schiller. Reconstruction of nuclear charged fragment trajectories from a large-gap sweeper magnet. *Nuclear Instruments and Methods in physics Reserach A*, 580, 2007.

[nsc]   http://www.nscl.msu.edu/[Online; accessed Mar-2014].

[RBFZ96]   C. M. Baglin S. Y. Frank Chu R. B. Firestone, V. S. Shirley and J. Zipkin. Table of isotopes, 1996.

[Sat12]   Y. Satou.   One-neutron knockout cross sections for 24o and 23o beams. Technical report, 2012. http://ribf.riken.jp/ysatou/r405n/sigma1n2423o.pdf.

[SFB$^+$07]   A. Schiller, N. Frank, T. Baumann, D. Bazin, B. A. Brown, J. Brown, P. A. DeYoung, J. E. Finck, A. Gade, J. Hinnefeld, R. Howes, J.-L. Lecouey, B. Luther, W. A. Peters, H. Scheit, M. Thoennessen, and J. A. Tostevin. Selective population and neutron decay of an excited state of o23. *Phys. Rev. Lett.*, 99:112501, Sep 2007.

[she]   http://www.nscl.edu/brown/sde.htm[Online; accessed Mar-2014].

[TB06]   J. A. Tostevin and B. A. Brown. Diffraction dissociation contributions to two-nucleon knockout reactions and the suppression of shell-model strength. *Phys. Rev. C*, 74:064604, Dec 2006.

[Tos01]   J. A. Tostevin.   Single-nucleon knockout reactions at fragmentation beam energies. *Nuclear Physics A682*, 32Oc-331c, 2001.

[Tos07]   J. A. Tostevin. Reaction spectroscopy at fragmentation beam energies recent advances in studies of two-nucleon removal. *The European Physical Journal Special Topics*, 150(1):67–70, 2007.

[Tos12]   J. A. Tostevin. Direct reaction probes of single-particle states and correlations. *Progress of Theoretical Physics Supplement*, 196:275–282, 2012.

[TPB⁺00] P.G Thirolf, B.V Pritychenko, B.A Brown, P.D Cottle, M Chromik, T Glasmacher, G Hackman, R.W Ibbotson, K.W Kemper, T Otsuka, L.A Riley, and H Scheit. Spectroscopy of the 21+ state in 22o and shell structure near the neutron drip line. *Physics Letters B*, 485(13):16 – 22, 2000.

[TPBH04] J. A. Tostevin, G. Podolyák, B. A. Brown, and P. G. Hansen. Correlated two-nucleon stripping reactions. *Phys. Rev. C*, 70:064602, Dec 2004.

[XW99] D. Johnson F. Marti R.C. York X. Wu, H. Blosser. the k500-to-k1200 coupling line for the coupled cyclotron facility at the nscl, 1999. 1999 Particle Accelerator Conference, New York.